INTERFACIAL STUDIES OF ALKYLATED GRAPHENE OXIDES USING LANGMUIR

BLODGETT AND

DIRECT INK WRITING OF POROUS SHAPE MEMORY POLYMERS

A Thesis

by

GREESHMA CHATHAMKANDATH RAGHUVARAN

Submitted to the Graduate and Professional School of
Texas A&M University
in partial fulfillment of the requirements for the degree of

MASTER OF SCIENCE

Chair of Committee,	Emily Pentzer
Committee Members,	Qing Tu
	Lei Fang
Head of Department,	Ibrahim Karaman

May 2023

Major Subject: Materials Science and Engineering

ABSTRACT

This thesis is composed of two studies. The first study investigates the interfacial properties of alkylated graphene oxide nanosheets using Langmuir-Blodgett techniques. The second study examines the direct ink write (DIW) additive manufacturing of linear polycaprolactone diacrylate shape memory polymers with generated porosity for ultimate applications in bone scaffolds. Below are summaries of each study.

In recent years, there has been an increasing interest in developing functionalized graphene oxide nanosheets as stabilizers for pickering emulsion systems. Alkylated graphene oxide nanosheets can be used to stabilize pickering emulsion systems, and are notable for the broad range of compositions that can be used (oil/water, oil/oil, and ionic liquid/oil). The purpose of this study is to understand the various parameters that influence the surface interactions of these nanosheets, in complement to the emulsion systems. Langmuir Blodgett experiments are conducted to identify the impact of alkyl chain lengths used for functionalizations, the effects of the solvent used for deposition, and the pH and ionic concentration of the liquid subphase. The interfacial phase transformations involved are compared to the maximum surface pressure and the onset of surface potential measurements while trying to determine the effect of various experimental parameters involved. The solvent used for sample dispersion as well as the alkyl chain length used for the sample functionalization both impact the interfacial nanosheet interactions. Emulsions being a two-phase system, different modifications to the trough medium were also generated through varying pH and subphase salt concentration to gather insights on how this would impact the behavior of different nanosheets on the interface. These variables were not identified to significantly impact nanosheet interactions.

The efficiency of bone scaffold implants in curing bone defects is dependent on their suitable fit, osteoinductivity, degradation properties, and biocompatibility. In the second part of the study, direct ink write (DIW) additive manufacturing is employed to print linear polycaprolactone diacrylate shape memory polymers with generated porosity for ultimate applications in bone scaffolds.

The ink generated for printing is rheologically modified through the addition of sodium chloride (NaCl) particles, which are sacrificial and removed via washing with water thus generating micropores in the structures. The use of printing gives additional flexibility in the construction of macropores through print design. Salt particles with a size of less than 38 microns are utilized to induce shear thinning characteristics in the polymer solution, which is then printed and cured using UV radiation. After the printing and curing phases, the salt particles are subsequently removed to create porosity. The printed structures with porous features and shape memory capability are subjected to further analysis to investigate their compositional, thermal, mechanical, and shape memory properties. This study focuses on the direct ink writing (DIW) process of these polymers and examines the ink composition to understand the effects of different factors on the properties of the printed objects. Several steps are taken to achieve desirable features, and a comprehensive analysis is carried out to investigate how each parameter impacts the properties of the printed objects.

DEDICATION

To my mother and father for letting me come this far. To my grandfather who remains in our memories and my grandmother who has let go of her memories. To my love, my inner strength though miles away, inspires me to work everyday. To the almighty for walking every mile of my life with me.

ACKNOWLEDGMENTS

CONTRIBUTORS AND FUNDING SOURCES

Contributors

Funding Sources

NOMENCLATURE

LB	Langmuir Blodgett
GO	Graphene Oxide
rGO	Reduced Graphene Oxide
C3-GO	Propylamine functionalized Graphene Oxide
C6-GO	Hexylamine functionalized Graphene Oxide
C9-GO	Nonylamine functionalized Graphene Oxide
C18-GO	Octadecylamine functionalized Graphene Oxide
DMF	Dimethylformamide
$CHCl_3$	Chloroform
BAM	Brewster Angle Microscopy
SMP	Shape Memory Polymer
DIW	Direct Ink Writing
PCL-DA	Polycaprolactone Diacrylate
DMP	2,2-Dimethoxy-2-phenylacetophenone
NaCl	Sodium Chloride
NMP	N-Methyl-2-pyrrolidone
THF	Tetrahydrofuran
SEM	Scanning Electron Microscopy
TGA	Thermogravimetric Analysis
FTIR	Fourier Transform Infrared Spectroscopy
DSC	Differential Scanning Calorimetry
DMA	Dynamic Mechanical Analysis
EDS	Energy-dispersive X-ray Spectroscopy

TABLE OF CONTENTS

LIST OF FIGURES

LIST OF TABLES

1.   INTRODUCTION

1.1   Interfacial Studies of Alkylated Graphene Oxides using Langmuir Blodgett

Emulsion stabilization studies have proceeded through various advancements in surfactants, from using particles as surfactants in Pickering emulsions to further replacing them with nanosheets for better coverage. Graphene oxide (GO) is commonly used to stabilize different oil-water systems, and simple functionalizations enable a broader range of emulsion compositions to be stabilized. In 2017, Rodier et al. demonstrated how alkyl amine functionalized GO can stabilize oil-in-oil emulsions and that the identity of the dispersed phase is determined by alkyl chain length; for example, GO modified with octadecylamine could stabilize DMF-in-octane emulsions, whereas GO modified with hexylamine could stabilize octane-in-DMF emulsions. [2] Further, in 2018 Luo et al. demonstrated the ability of GO to stabilize ionic liquid-in-water emulsions, and for octadecylamine modified GO to stabilize ionic liquid-in-oil emulsion systems. [3] However, there still exists a knowledge gap in understanding the underlying phenomena of stabilization and how different parameters influence the system, such as how the nanosheets interact at the fluid-fluid interface and how this changes the interfacial tension of the system.

A Langmuir Blodgett (LB) trough is an instrument widely used to prepare and study monolayers of various systems [4] such as small molecule and polymeric surfactants. In 1994, Chou et al. used LB to determine the orientation of the porphyrin macrocycle by relating the surface pressure isotherms to interactions between the molecular structures and the aqueous phase. [5] Further, in 2006, Wen et al. explored the effects of non-selective and selective solvents in the spreading of diblock copolymers atop the water, to discover labyrinth-like morphologies at the air-water interface. [6] These indicate how the versatility of Langmuir Blodgett studies could open opportunities for answering various questions concerning particles at interfaces. [7]

In addition to small molecules and polymers, LB techniques can be used to compress or transfer monolayers of nanosheets and thus is capable of conducting fundamental supramolecular chem-

istry studies. Specifically, LB of graphene oxide was used to generate monolayers [8], inspect various morphology formations [9], and create composites [10] and functional devices [11] in the past. In 2008, Cote et al. successfully demonstrated the formation of stable GO monolayers on the LB trough interface. In this study, the electrostatic repulsion that exists between layers was held responsible for preventing coagulation without any stabilizing agent. [8] In 2010, Kulkarni et al. utilized the GO nanosheets formed from LB to fabricate polyelectrolyte multilayer-based nanocomposites. The addition of 8 vol% of LB deposited GO achieved an elastic modulus 13 times larger than what a layer-by-layer deposited GO can achieve. [10] In 2012, Zheng et al. synthesized ultra-large GO nanosheets using an LB trough and achieved flat, rippled, collapsed, folded, and curved morphologies in their deposition. [9] Further, in 2014, Yang et al. demonstrated employing reduced GO films from the LB technique to improve the luminance performance in organic light-emitting diodes. [11]

LB studies generally make use of a monolayer of amphiphilic surfactants at the air-water interface, the hydrophilic or polar part interacting with the aqueous subphase and the hydrophobic part extending to the air medium. However, exceptions to this have been reported in the past where stronger inter-molecular interactions generate "non-traditional Langmuir monolayers" where strongly H-bonded groups face the air, forcing the hydrophobic part to be immersed in water. [12] In this study, the hydrophilicity of graphene oxide nanosheets is manipulated through different alkyl chain functionalizations to generate varying behaviors at the interface (Figure 1.1).
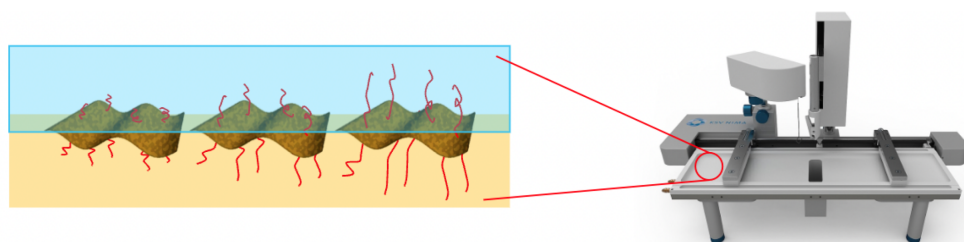
Figure 1.1: Alkyl chain functionalized graphene oxide nanosheets at LB trough interface.

1.2 Direct Ink Writing of Shape Memory Polymers

Synthetic bone scaffold implants are widely used in the treatment of bone defects. While these bone scaffolds require to have desirable biodegradable, osteogenetic[1], degradation, and porosity properties, their bone-to-graft ratio[2] determines their efficiency in curing bone defects. While there has been a lot of progress made in catering the implants to fit the shape of the defect itself, it is a dynamic cavity. Shape memory polymers (SMPs) are a class of interesting functional materials that are capable of modifying their shape in response to an external stimulus. Based on the polymer structure, the stimulus could be thermal, optical, or electrical. In a thermally stimulative SMP, while the base shape of these structures is defined at room temperature, heating the structure to a transition temperature can facilitate stretching, bending, and twisting to any desired shape. The modified shape is retained when cooled down to room temperature and remains until the same thermal stimulus is provided to retrieve the base structure. Due to this possibility to shapeshift, SMPs are desirable for use in biomedical implants. [13, 14] Given the ease of inserting them into the human body by heating them to mild temperatures, they are capable of taking the exact shape of the bone defect once cooled down to the normal human body temperatures and retaining this shape permanently. [15]

Polycaprolactone is a biodegradable polymer prominently used to fabricate human body implants and has been shown to have favorable degradation rates. [16], [17] In 2014, Zhang et al. successfully employed a shape memory polycaprolactone-diacrylate (PCL-DA) polymer to generate porous scaffolds to treat cranio-maxillo facial bone defects. Further, Pfau et al. attempted to improve the self-fitting properties of the scaffolds with the addition of linear-poly(L-lactic acid), employing star and linear morphology combinations. [18] In these systems, a fused salt template is used to generate the porous structure. The template is created by adding size-optimized sodium chloride particles in a glass vial with distilled water, centrifuging the mixture, and drying the vials in air and vacuum. However, the system suffers from a lack of flexibility to generate more complex

---

[1]related to the formation of bone
[2]the area of contact the scaffolds can maintain with the surrounding tissues

geometries as the template containers limit the shape of these scaffolds.

Direct ink writing (DIW) is a form of 3D printing based on the extrusion of a purpose-based liquid mixture referred to as 'ink' that is tailorable for a vast range of applications. Unlike many forms of 3D printing that require heating the sample, DIW does not require any thermal heating and is suitable for biomaterials [19–21] and other temperature-sensitive materials. The ink suitability to DIW is merely dependent on its rheology and requires shear thinning and thixotropic properties. In 2021, Cipriani et al. showed how to use paraffin wax beads to modify the rheology of DIW ink, which could be washed away using ethyl acetate post-printing, to generate pores. [22] Studies were conducted to observe what proportions of the sacrificial filler in the matrix are effective and defective towards ink printability. In 2022, Cipriani et al. also successfully demonstrated the use of non-sacrificial fillers like fluid-filled particles in DIW. [23] The selection of filler material for a printed object must be customized based on the intended use and whether the filler serves any necessary purpose for the final product.

In previous studies, the PCL-DA polymer has exhibited shape memory properties but has been deemed unsuitable for extrusion in DIW due to its tendency to form a Newtonian fluid when dissolved in a solvent. However, in 2022, Wei et al. successfully demonstrated the potential of incorporating sodium chloride (NaCl) into the DIW ink and utilizing a water-washing process to generate porosity in printed structures while modifying the rheology of the ink to shear-thinning. [24] Further, NaCl being a naturally occurring compound and essential mineral in the human body, makes it an ideal filler for bone scaffolds. Therefore, the integration of DIW with sacrificial NaCl filler to print PCL-DA presents an opportunity to produce porous shape memory polymers for various applications, including biomedical engineering.

4

2. INTERFACIAL STUDIES OF ALKYLATED GRAPHENE OXIDES USING LANGMUIR BLODGETT

2.1   Research Objectives

In this project, the different system parameters that influence an emulsion's stability are probed through various interfacial studies conducted on alkylated graphene oxides using Langmuir Blodgett. The behavioral patterns of the nanosheets at the interface with varying alkyl chain lengths, solvents of dispersion, and the surrounding medium factors are studied. This is carried out by observing the pressure isotherm measurements and associated interfacial phase transformations that take place in the system upon compression of the deposited nanosheets. By considering the precise variations brought into the system through various experimental and instrumental parameters, an attempt to create a more holistic understanding of the system is made. Although the air-water interface obtained in the LB trough is not the ideal translation of a liquid-liquid interface present in emulsions, the isotherm measurements are expected to provide insights into the stabilization of a spectrum of interfaces.

2.2   Experimental Details

2.2.1   Materials

Graphene Oxidec(GO) for the experiments was synthesized using the modified Hummer's process. Alkylated Graphene oxides, namely propylamine graphene oxide (C3-GO), hexylamine graphene oxide (C6-GO), nonylamine graphene oxide (C9-GO), and octadecylamine graphene oxide (C18-GO) were synthesized by functionalizing GO using propylamine (C3-NH$_2$), hexylamine (C6-NH$_2$), nonylamine (C9-NH$_2$) and octadecylamine (C18-NH$_2$) respectively. Triethylamine ((C$_2$H$_5$)$_3$N) was used to synthesize reduced graphene oxide (rGO) using a similar mode of synthesis. The method of synthesis and functionalization are discussed in detail in Appendix A.

Octadecylamine was purchased from Oakwood Chemical, hexylamine from Thermo Scientific, and propylamine, nonylamine, and triethylamine from Sigma Aldrich. The functionalized samples

were dispersed in four different solvents, namely chloroform ($CHCl_3$), toluene, ethyl acetate, and dimethylformamide (DMF), all of them acquired from Sigma Aldrich in HPLC grade and used as received.

For the latter part of the study, pH buffer solutions corresponding to a pH of 4.4 and 10.2 were synthesized in the lab. The synthesis method is detailed in Appendix A. For this purpose, sodium carbonate was purchased from Sigma Aldrich, sodium hydroxide from Oakwood chemical, and sodium bicarbonate and acetic acid from Fisher Chemical. The chemicals were used as received. Further, sodium chloride (NaCl) used to modify the subphase ionic concentration was purchased from Fisher Chemical and the MXene used in the study was obtained from Huaixuan Cao et al. as reported previously. [25]

2.2.2 Instrumentation

A KSV NIMA medium LB trough (273 cm^2 surface area, 10.8 maximum compression ratio, 0.03 μN/m balance resolution) was used for the measurements. The instrument was operated with a barrier speed of 30 mm/min and the trough was filled to an approximate volume of 250 ml of distilled water prior to aspiration and maintained at this volume throughout all experiments. A KSV NIMA MicroBAM (50 mW light source power, 659 nm light wavelength, 12 μm image resolution, 3600 x 4000 μm field of view) was used to capture the in-situ images of the sample interactions.

2.3 Methods

2.3.1 Sample Preparation

Alkylamine modified GO nanosheets, namely propylamine graphene oxide (C3-GO), hexylamine graphene oxide (C6-GO), nonylamine graphene oxide (C9-GO), octadecylamine graphene oxide (C18-GO) and reduced graphene oxide (rGO) are employed in this interfacial study with Langmuir Blodgett. There was maximum care provided to avoid the presence of excessive alkylamine small molecules in the dispersion and later in the trough interface as they can generate discrepancies in the acquired results. The supernatant from the washing of the alkylated GO sam-

6

ples was collected after each round, and the solvent was removed by evaporation to collect the residue and analyzed using FTIR. Having confirmed the alkylamine presence in them, washes were carried out until the amount of residue generated was reduced to negligible quantities. The method employed in removing the small molecules from the samples is explained in Appendix A.

For further experiments, the pH of the LB trough subphase was controlled by substituting distilled water in the subphase with acidic (pH 4.4) and basic (pH 10.2) buffer solutions. The procedure for the synthesis of the buffer solutions is provided in Appendix A. In a similar manner, different aqueous solutions of varying sodium chloride concentrations were prepared to be used in the trough subphase. The MXenes obtained had a concentration of 14 mg/ml and were dispersed in water. After a few failed attempts to centrifuge out water even combined with other solvents, the MXene solution was vacuum dried and redispersed in DMF in a concentration of 1 mg/ml.

2.3.2 LB Trough Preparation, Nanosheet deposition, and Compression

The surface pressure isotherm measurements were carried out using the Langmuir Blodgett instrument. The LB trough consists of a trough top and two barriers attached to a frame, as well as a surface pressure sensor that should be partially immersed in the base medium to record pressure variations during experiments. The trough top and barriers are rinsed separately multiple times using distilled water and isopropyl alcohol before loading to the experimental setup. Afterward, excess water is wiped off smoothly only from the metallic parts (parts that do not come in contact with the sample or trough medium during a run). The trough was filled with exactly 250 ml of distilled water before aspiration for all experiments and any impurity present on the surface is aspirated, to keep the base surface pressure < 0.2 mN/m, to begin with. Further, barriers are employed to compress and relax the surface of the water and the nanosheet dispersion is carefully dispensed between the barriers on the air-water interface using a microsyringe. The samples post-synthesis were each adjusted to a concentration of 1 mg/ml and approximately 50 μl of the sample was dispensed for each analysis. A platinum Wilhelmy plate is used for the pressure measurements that capture various interactions between the nanosheets. Each LB result presented below is generated by averaging at least three LB runs, to establish reproducibility. Table 2.1 summarizes all

the parameters used in the experiments conducted.

Experimental Parameters	Experimental Condition/Value
Trough Subphase	Distilled water, 250 ml
Compression Range	0 mm to 140 mm
Baseline Maintained	< 0.2 mN/m
Sample Concentration	1 mg/ml
Sample Dispensed	50 µl
Barrier Speed	30 mm/min
Pressure Measurement	Platinum Wilhelmy Plate

Table 2.1: Langmuir Blodgett Parameters and Experimental Conditions

Nanosheet particle behavior on the trough surface generates interfacial phase transitions. The same is depicted in (Figure 2.1) where the surface pressure is plotted against the surface area per molecule (adapted from [1]). An illustration is provided to demonstrate how surfactant molecules arrange themselves at the interface, leading to the observed interfacial phase transitions (the image is obtained from Biolin Scientific). The pre-interaction stage between the nanosheets results in a two-dimensional gaseous phase, where they are free to move around without any force intrusion. Initiating barrier compression, the particles start interacting horizontally over the edges and start exerting force on each other. This stage still maintains fluidity in the nanosheet movement and is regarded as the liquid phase. According to the amphiphilic molecules used and the temperature, there could be two categories within the liquid phase, namely the liquid-expanded and liquid-condensed phases. When compressed further, the movement of the nanosheets is hindered completely and hence reaches the solid phase. Further compression might lead to nanosheets collapsing leading them to stack on each other and also climb onto the Wilhelmy plate in certain scenarios. These stages of interfacial phase transitions can be identified through slope patterns in the pressure isotherms and can be employed to draw insights into different categories of particle

interactions.
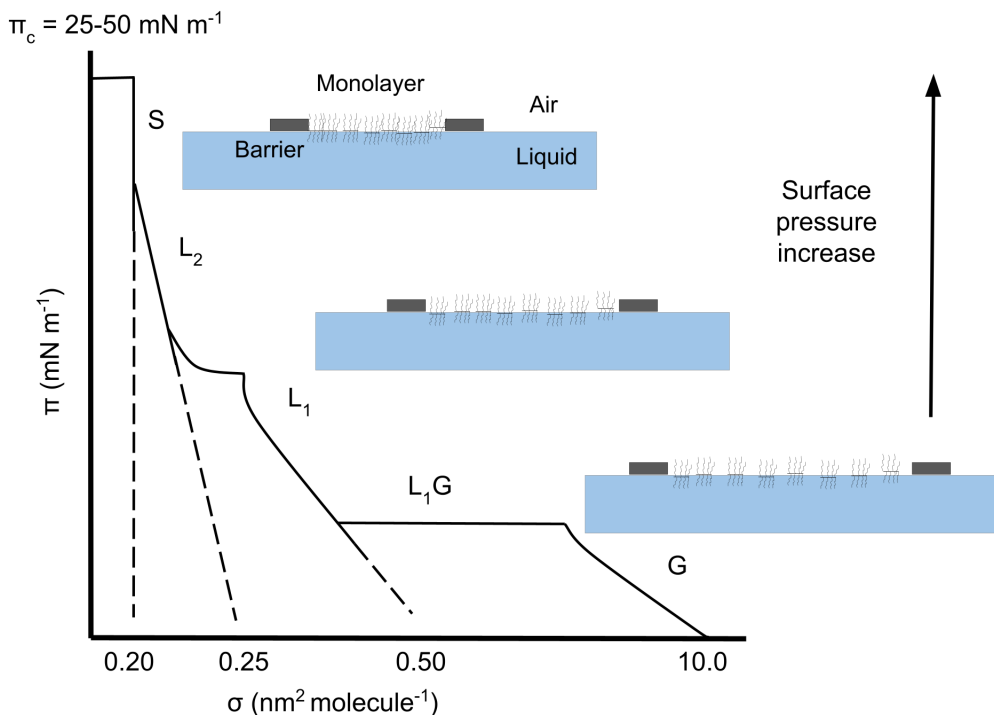
Figure 2.1: Interfacial phase transitions depicted in a surface pressure-area isotherm.
(adapted from [1])

The quantity of the sample dispensed for the studies (50 μl) might be pointed to as insufficient for drawing quantitative conclusions according to certain previous studies. [8] However, this is observed to be sufficient to attain the solid phase and even stacking phases pertaining to nanosheet phase transition interactions. Hence, any larger quantity would have had most of the sample sink to the bottom of the trough. This might contribute to minor modifications in the trough medium itself and interfere with the results.

2.3.3   Brewster Angle Microscopy (BAM)

BAM images of the nanosheets were captured at various points of compression to create a better understanding of how the nanosheets are organized at the interface. These images were used to correlate the pressure isotherm measurements with the phase transformations associated with the nanosheet interactions.

9

2.4 Results

In alkylated graphene oxides, the surface interactions of the nanosheets are prominently influenced by the alkyl chain attachments around them. The onset barrier position, peak pressure, and hysteresis of isotherm measurements were observed to reflect the behavior induced by the length of alkyl chains around these nanosheets. These interactions are also at the same time affected by the solvent of dispersion. The effect of alkyl chain lengths combined with the solvent of dispersion in the LB experiments is discussed in more detail in the coming sections. An attempt is also made to understand the influence of the aqueous subphase on the nanosheets' interfacial behavior, by varying the pH and the salt concentration in the trough medium.

2.4.1 Interfacial Phase Transitions of Nanosheets

The interfacial phase transformations that alkylated GO nanosheets undergo at the LB trough surface were analyzed using BAM. The BAM images of C18-GO, C12-GO, and C6-GO dispersed in CHCl$_3$ at various ranges of compression are presented below in Figure 2.2. However, due to space restrictions, it is not possible to install both BAM and Wilhelmy plate in the LB trough simultaneously. Moreover, capturing BAM images at higher rates of compression is challenging for similar reasons. These limitations make it difficult to probe the nanosheet interactions while surface pressure isotherm measurements are being carried out. Conducting both measurements at different times does not ensure a direct comparison, which hinders the ability to draw meaningful conclusions about the process.
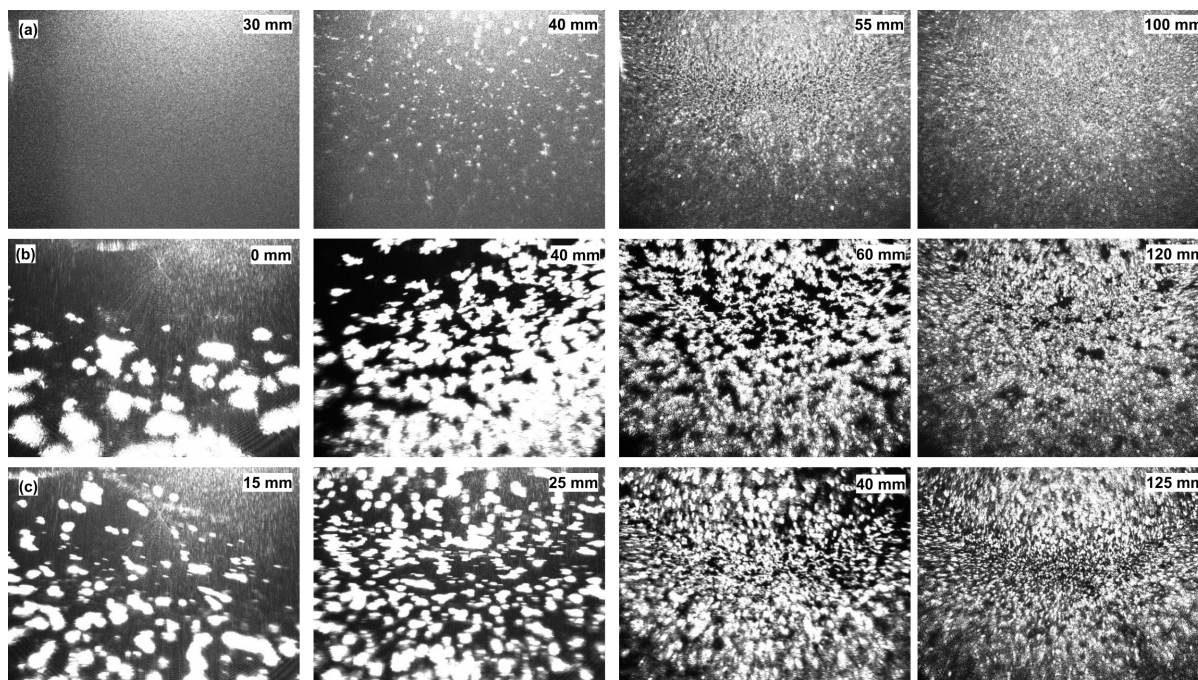
Figure 2.2: BAM images of (a) C6-GO, (b) C12-GO and (c) C18-GO nanosheets on the LB trough at different lengths of compression as indicated.

2.4.2 Impact of Sample Dispersion Medium

To probe the effect of different dispersion solvents in the alkylated nanosheet interactions, octadecylamine functionalized graphene oxide (C18-GO) dispersed in $CHCl_3$ and toluene were examined using an LB trough. Alongside observing the discrete behavior of C18-GO in these solvents, additional experiments were run on samples generated from different proportional combinations of these dispersions. 50 µl of each sample was dispensed on the trough surface, allowed to stabilize, and further compressed through 140 mm on both sides by the barrier attachment. The surface pressure, which remains almost zero, starts exhibiting a rise as the nanosheets start interacting horizontally. As you can observe from Figure 2.3, this interaction begins early when C18-GO is dispersed in $CHCl_3$ (~57mm) compared to toluene (~108mm). Reaffirming the same, all the other proportions lie in between the pure solvents and show an increasing pattern of onsets, starting from chloroform with an increasing proportion of toluene. As the compression of nanosheets continues, there is a change in the rate of pressure increase, indicating the gaseous-to-liquid and

11

liquid-to-solid interfacial phase transitions. They also follow the same pattern: nanosheets undergo phase transitions earlier in chloroform than in toluene. Since the same C18-GO sample is dispersed in both solvents, the hypothesis is that C18-GO dispersed in chloroform exhibits better spreading of alkyl chains at the interface compared to when dispersed in toluene.
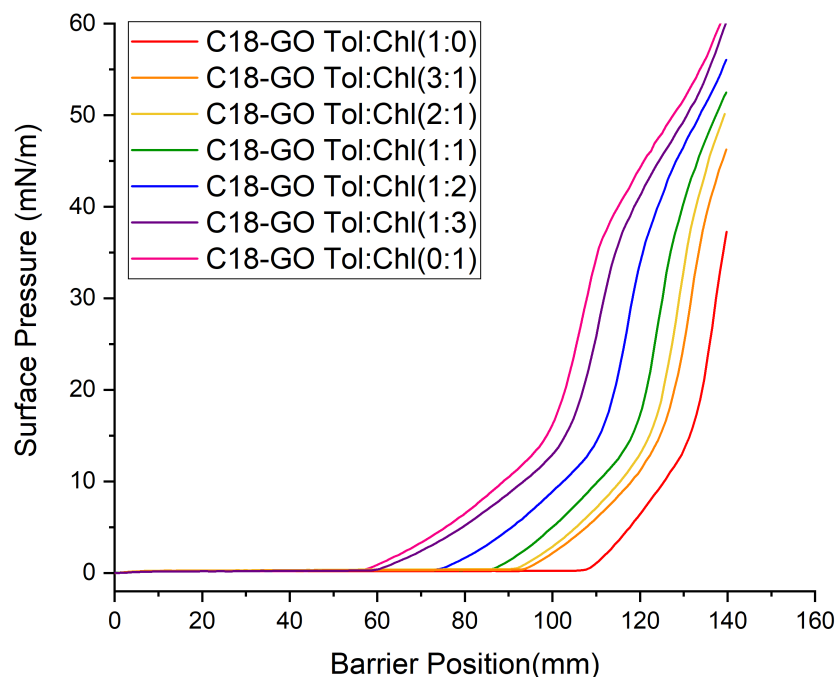
Figure 2.3: Surface pressure isotherms of C18-GO dispersed in a combination of chloroform and toluene solvents.

To confirm that the differences in pressure-area isotherms are in fact attributed to the nanosheet configurations, the possibility of nanosheets dispersed in one or more solvents sinking to the trough bottom during barrier compression need to be ruled out. To ensure all nanosheets were floating atop the water (and no nanosheets were transferred to the subphase), C18-GO was compressed to 85% of maximum compression (120 mm) and held for 10 mins with both the solvents of dispersions to facilitate any sinking if feasible (Figure 2.4).

Sinking behaviour: Nanosheets sink to the bottom under compression, modifying the surface pressure isotherm on further compression

Non-Sinking behaviour: No nanosheet sink to the bottom under compression, maintaining the surface pressure isotherm on further compression
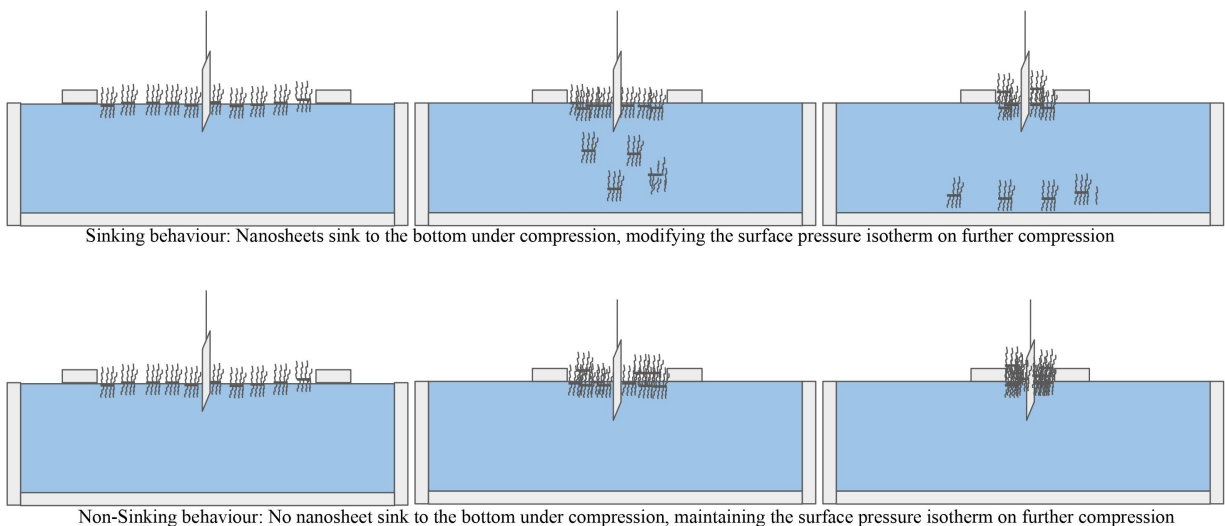
Figure 2.4: Possible sinking (top) and non-sinking (bottom) behavior of nanosheets during the compression hold.

Despite holding at the compressed state, continuing the barrier compression after the hold resulted in the same peak pressure and isotherm path in these samples (Figure 2.5), confirming no sinking. Alternatively, if sinking had taken place, the sample would not regain the surface pressure it would have attained with continuous compression at the maximum compression length i.e, 140 mm. Hence, all the nanosheets remain at the interface during our study and the difference in the alkylated nanosheets' behavior was solely generated by the solvent of dispersion.
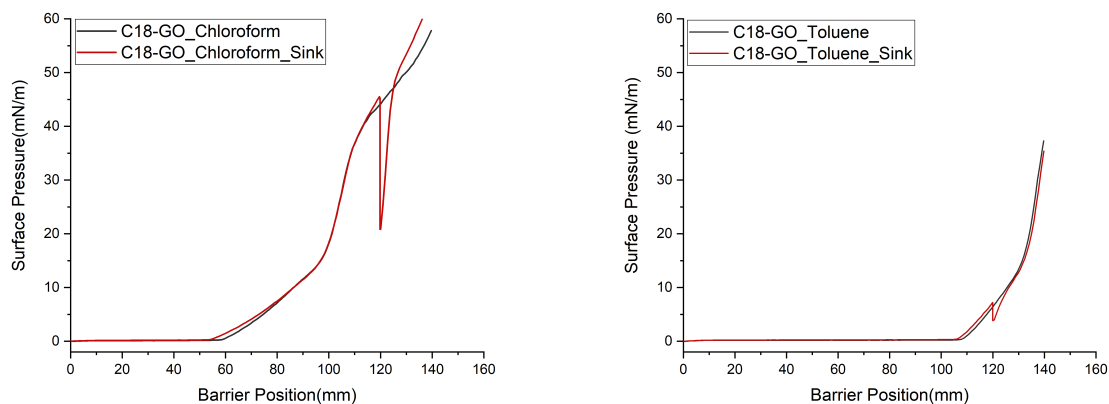
Figure 2.5: Sinking behavior study of C18-GO dispersed in CHCl$_3$ or toluene.

Further, rGO, C3-GO, C6-GO, and C9-GO were dispersed in four different solvents to conduct pressure isotherm measurements. The study considers four solvents: chloroform, ethyl acetate, toluene, and dimethylformamide. The pressure isotherms of various alkylated GO samples in different solvents are shown below (Figure 2.6). The plots denote an average of three very agreeing results under each sample, belonging to the respective functionalization and solvent of dispersion.

Chloroform is a solvent that is capable of dissolving the alkylamines effectively and hence provides good dispersion of nanosheets on the surface of the water. Hence you can see how all the alkylated samples exhibit a peak higher than 30 mN/m and achieve an onset lesser than 130 mm. The exception here is reduced graphene oxide which contains no alkylamine chains and hence fails to have any major interaction in chloroform in the used amount and concentration.

14
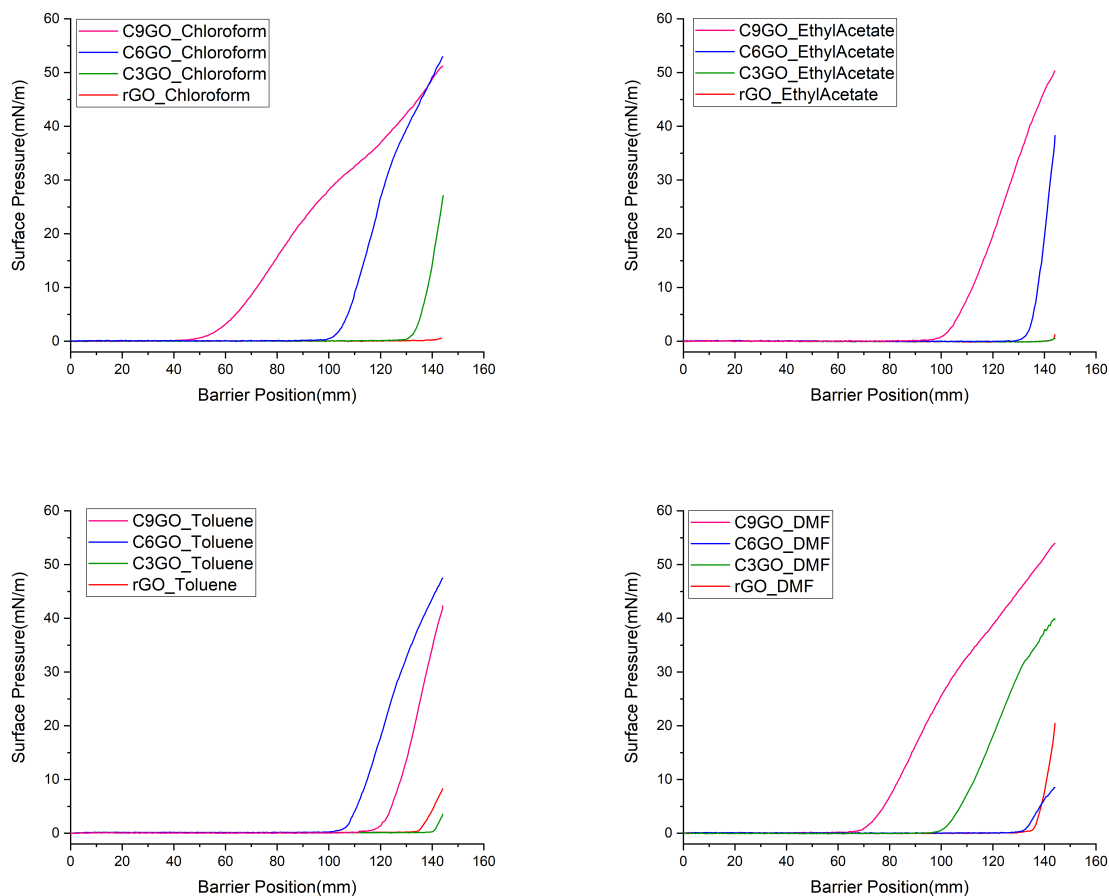
Figure 2.6: Surface area-pressure isotherms of rGO, C3-GO, C6-GO, and C9-GO dispersed in chloroform, toluene, ethyl acetate, and dimethylformamide.

Toluene and ethyl acetate generate almost similar results with the alkylate GO nanosheets. The higher-length alkyl chains, C9 and C6 exhibit peaks higher than 40 mN/m and achieves an onset before maximum compression is reached in the range of 100-135 mm. Now, C3-GO and rGO both exhibit poor nanosheet interactions in these solvents. They do not achieve any significant peak surface pressure until maximum compression (140 mm). This is indicative of how individual solvent characteristics and their interaction with each sample play a role.

Finally, dimethylformamide (DMF) is a solvent capable of dispersing rGO unlike the other solvents but does not exhibit the best stability in dispersing alkylated GO, especially with longer

15

alkyl chains. However, DMF generates pressure isotherms where the interaction is intermittently aided by the alkyl chains and solvent effect giving rise to mixed patterns. While the higher length of alkyl chains like in C6-GO struggle to start interacting until 130 mm compression and to achieve a peak higher than 10 mN/m, samples with shorter or no alkyl chains tend to interact at lower compression stages and show higher peak pressures or a combination of both.

2.4.3   Impact of Alkyl Chain Lengths

The onset of surface potential barrier positions and the surface peak pressure values pertaining to the solvent variations and alkyl chain length differences are listed in Table 2.2 below. Seeing the same results above from the perspective of alkyl chain lengths, the following observations can be made. C9-GO with the longest alkyl chain was found to exhibit a high peak pressure in the range of 40-55 mN/m and attains the onset of surface potential before 100 mm of compression irrespective of the solvent it was dispersed in. This could be attributed to how nonylamine possesses the optimum chain length to spread out in most solvents and impact the interaction on the interface. The isotherms from C6-GO maintain similar peak surface pressure results in chloroform, toluene, and ethyl acetate. However, C6-GO exhibits a significant drop in the peak value in DMF. Also, coming to nanosheet interactions, the onset of surface potential in C6-GO only happens at higher extents of compression in both DMF and ethyl acetate. To make a direct conclusion on whether this is produced solely from the alkyl chain length, the number of nanosheets dispersed on the interface must be quantifiable. This is close to impossible with graphene oxide even when the mass concentration of the samples is kept constant attributed to the varying size of nanosheets and associated functionalizations.

Sample/Solvent	Peak Pressure (mN/m, top) Onset Barrier Position (mm, bottom)			
	CHCl$_3$	Toluene	Ethyl Acetate	DMF
C9-GO	51	41	51	55
	65	100	100	70
C6-GO	51	51	41	12
	100	100	135	130
C3-GO	31	3	3	37
	120	140	140	130
r-GO	1	6	3	22
	140	140	140	140

Table 2.2: Peak pressure and onset barrier position of rGO, C3-GO, C6-GO, and C9-GO dispersed in chloroform, toluene, ethyl acetate, and dimethylformamide.

In C3-GO, a comparatively stronger peak in the range of 30 mN/m is observed in DMF and chloroform solvents but a drop in peak pressure to 3 mN/m is observed when dispersed in toluene and ethyl acetate solvents. This is closer to the behavior of rGO, with the exception of the nanosheets being interactive in chloroform. rGO nanosheets almost exert no pressure on each other in solvents that fail to disperse it efficiently, that is all the solvents inspected with the exception of DMF. In DMF, rGO spreads out and interacts with each other in a manner detectable by the Wilhelmy plate thus producing a peak surface pressure of 22 mN/m although the onset of surface potential here is no earlier in the compression stages compared to other solvents.

Overall, it is not clear how these variables affect nanosheet interactions at the air-water interface. In summary, it is difficult to identify a clear trend regarding the impact of solvent variations and alkyl chain length differences on nanosheet interactions at the air-water interface. Each alkyl chain length-solvent combination appears to be unique and is influenced by multiple factors during the isotherm measurements.

2.4.4 Impact of Subphase pH

The effect of aqueous subphase pH on the behavior of nanosheets at the air-water interface was probed through studying four sets of samples in the LB trough. C9-GO and rGO in DMF and chloroform solvents were analyzed to understand how ionic and steric interactions in these systems affect the inter-nanosheet behavior. The LB pressure isotherm results obtained for these systems are shown in Figure 2.7.
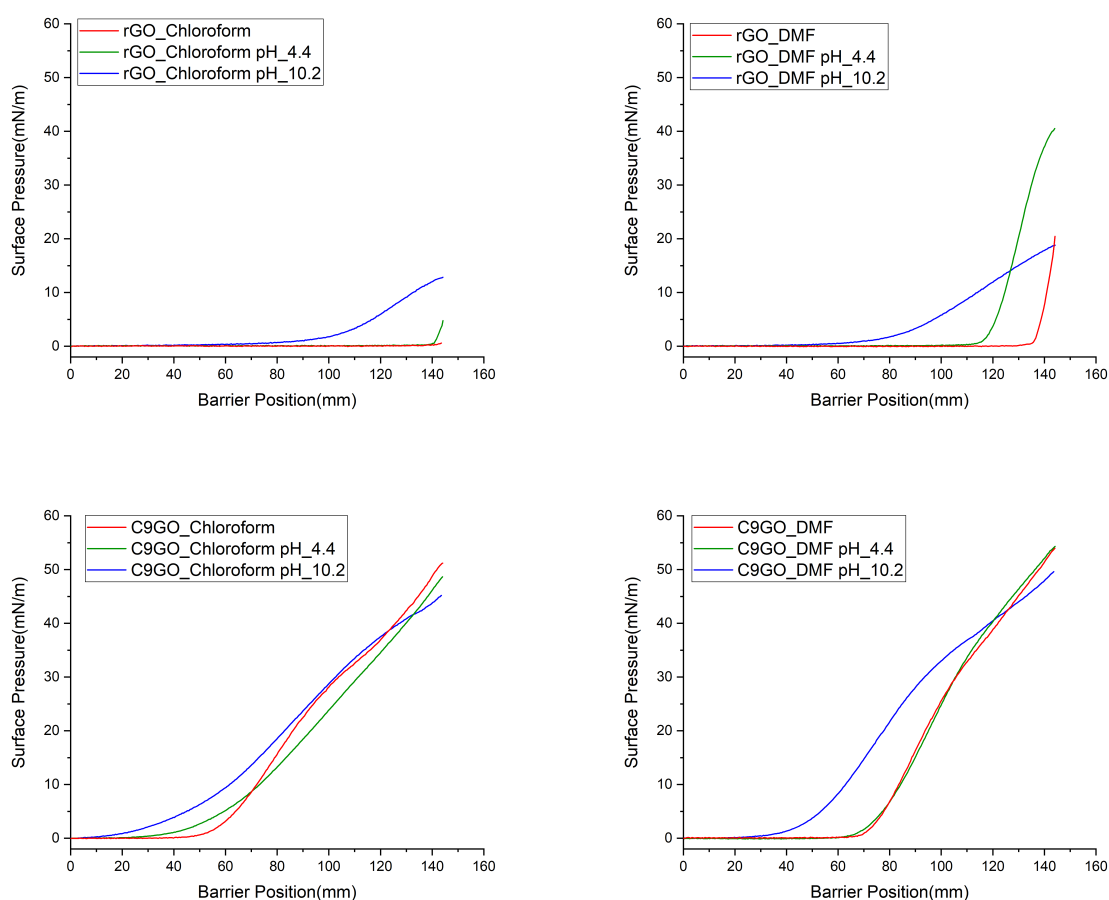
Figure 2.7: Surface pressure isotherms of rGO and C9-GO dispersed in chloroform, and DMF solvents under different pH subphases.

Previous pH subphase studies on LB trough have concluded that only the polar elements present on the interface are impacted by the pH variations that happen on the subphase, not the nonpolar parts. [26] Our acidic buffer is capable of releasing protons into the system as well as small quanti-

ties of hydroxide ions to neutralize the solution turning further acidic. C9-GO apart from the alkyl chain attachments also possesses the regular functionalization groups associated with graphene oxides like hydroxyl, carboxyl, carbonyl, epoxy, and ether on the basal plane and edges. Now, the protons from the buffer are capable of interacting with the functional groups surrounding C9-GO and could get attached to them. On the other hand, reduced graphene oxide has fewer of these functional groups on the surface and protons undergo lesser to no attachments with the nanosheets. This leads to additional protons on the surface of the LB trough, crowding around with the existing rGO nanosheets leading to a higher surface peak pressure than the neutral medium and an earlier onset of surface potential. This is, however, more evident when dispersed in DMF, reflecting the rGO behavior in DMF and chloroform. However, C9-GO undergoes no evident change and maintains the same isotherm measurements. This could be attributed to the fact that the protons have joined the nanosheets that makeup C9-GO, resulting in a unified structure that is not significantly altered by the addition of protons.

From the basic buffer, hydroxyl and bicarbonate ions are assumed to have been released into the system. This leads to electrostatic repulsion generated with the hydroxyl, and carboxyl groups of graphene oxides or in general steric repulsions due to the size of ions generated. This leads to the reduction of onset values for all the samples. Specifically to C9-GO, the long alkyl chains attached to the nanosheets shield the GO functional group interaction with the buffer ions thus not leading to an increase in the surface peak pressure. Whereas in rGO, the absence of alkyl chains to shield this interaction causes the electrostatic interaction to take place with the remaining functional groups post-reduction and cause an increase in the peak surface pressure while dispersed in chloroform. However, in DMF, rGO is already present in the most dispersed form thus leaving little to no space for the buffer ions to come to the surface and interact with them. Hence, the pressure isotherm almost undergoes no changes. The peak pressure and onset barrier positions for the above isotherms are represented in Table 2.3 below.

Sample	Solvent/pH	Peak Pressure (mN/m, top) Onset Barrier Position (mm, bottom)		
		Neutral	Acidic	Basic
C9-GO	CHCl$_3$	51.2	48.6	45.4
		50	30	10
	DMF	54	54.3	49.8
		70	70	30
r-GO	CHCl$_3$	0.6	4.8	12.8
		140	140	60
	DMF	20.4	40.4	18.8
		135	110	50

Table 2.3: Peak pressure and onset barrier position of rGO and C9-GO dispersed in chloroform and dimethylformamide under different pH subphases.

The system being studied here includes various factors such as the presence or absence of alkyl chains, oxidation and reduction on the graphene surface, and the effect of the solvent dispersion medium. This leads to various steric and electric interactions between the buffer ions and the sample. Because of these complex factors, there could be multiple possible explanations for the behavior observed in the samples being analyzed. Having realized the complexity of this system, an attempt was made to simplify the system in the next section by inspecting the impact of neutral sodium chloride on the LB subphase.

2.4.5 Impact of Subphase Ionic Strength

pH variations in the subphase depends on various parameters including electrostatic and steric impacts, and changes in pH can lead to the chemical transformation of the nanosheets (including reduction or protonation). To overcome these effects, a system with fewer variations was considered. Pressure isotherm measurements were carried out in Langmuir Blodgett with varying salt concentrations in the medium. rGO and C9GO in DMF solvent were compared between different concentrations of NaCl dissolved in the subphase (Figure 2.8). The difference between plain

distilled water and 5 mM, 15 mM, 25 mM, and 100 mM NaCl salt concentrations in the subphase were compared. rGO shows a significant shift in the pressure isotherm behavior upon the introduction of salt in the subphase. With an increase in salt concentration, rGO shows earlier onsets and higher peak pressure. On the other hand, C9-GO shows no difference in these variables with the introduction of salt in the subphase. This may be attributed to the interactions in alkylated graphene oxides being dominated by the alkyl chains around the nanosheets and the size of salt molecules being negligible in comparison.
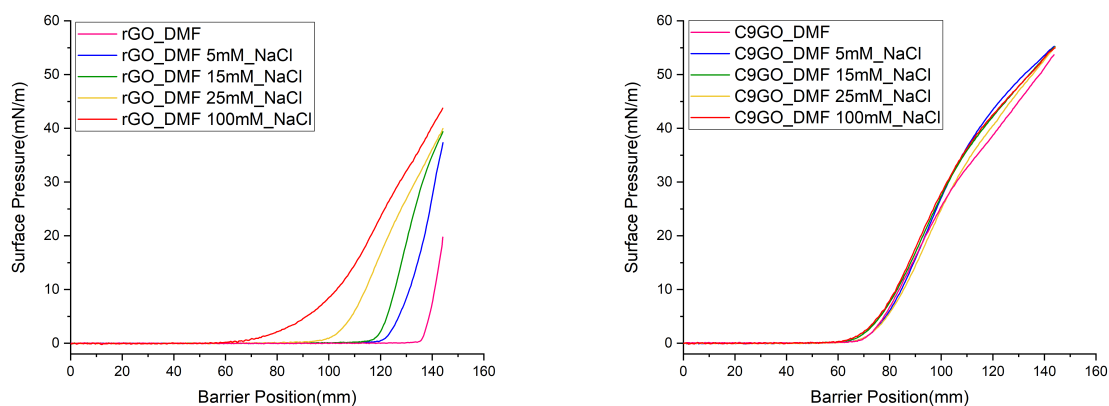
Figure 2.8: Surface Pressure Isotherms of rGO and C9-GO dispersed in DMF under different NaCl concentrations in the subphase.

Further, to inspect if the impact of subphase salt concentrations was general to nanosheets, transition metal carbides were evaluated in addition to graphene oxide in Langmuir Blodgett. Cao et al. in 2021 showed how sodium chloride salt addition to MXene sheets can adjust their zeta potentials leading to lesser repulsion and hence flocculation between the nanosheets. [25] Tuning the zeta potential using different salt concentrations and different ionic salts were inspected to show effective shielding of charges between the nanosheets and their dependence on the salt ionic radii and adsorption. However, even larger variations in the subphase salt concentrations fail to generate a noteworthy impact in the MXene LB pressure isotherms as shown in Figure 2.9. Studies were also extended to other salts like $MgCl_2$. Despite the ionic charge or molecular size difference of

the salts, the pressure isotherms of both salts were approximately overlapping. The peak pressure and onset barrier positions for the above isotherms are represented in Table 2.4 below. There is no possible explanation for this occurrence.
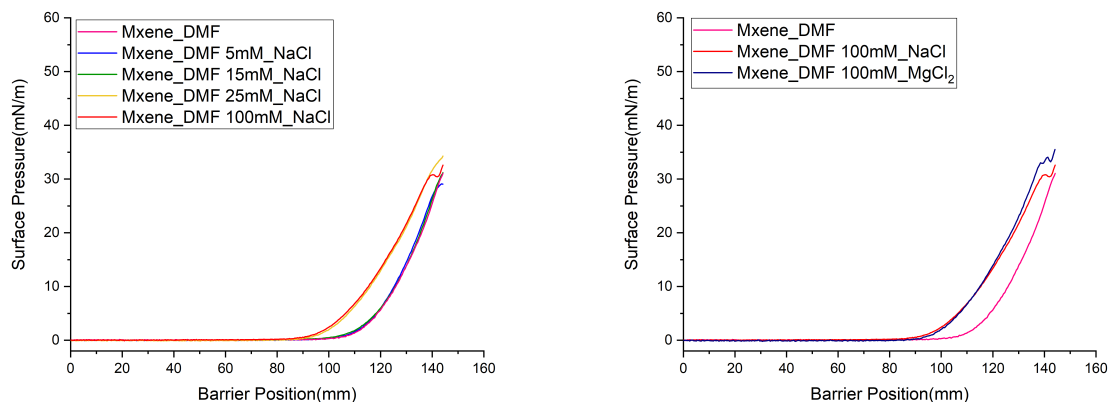
Figure 2.9: Surface pressure isotherms of MXene dispersed in DMF with different NaCl concentrations in the subphase (left), isotherms in NaCl, and $MgCl_2$ salt subphases (right).

	Peak Pressure (mN/m, top) Onset Barrier Position (mm, bottom)				
Sample/Solvent	0 mM	5 mM	15 mM	25 mM	100 mM
C9-GO	54	55.4	55.2	55.1	55.0
	70	70	70	70	70
r-GO	19.7	37.3	39.4	40	43.7
	135	120	115	95	65
MXene	31.1	29.1	31.2	34.3	32.7
	105	105	105	90	90

Table 2.4: Peak pressure and onset barrier position of rGO, C9-GO, and MXene dispersed in DMF under different subphase salt concentrations.

3. DIRECT INK WRITING OF SHAPE MEMORY POLYMERS

3.1 Research Objectives

The ink used in this study for DIW is composed of PCL-DA dissolved in an organic solvent and uniformly mixed with sodium chloride particles that act as both a rheology modifier and a porosity generator (Figure 3.1). The resulting ink displays shear-thinning properties that facilitate smooth extrusion, while its thixotropy enables the extruded part to retain its shape until crosslinks are created between the polymers during curing. Curing is achieved by UV light irradiation, aided by a photoinitiator that is included in the ink. After printing, the porosity generated by the filler particles and the print design is analyzed for their effects on the thermal, mechanical, and shape memory properties of the printed structures.
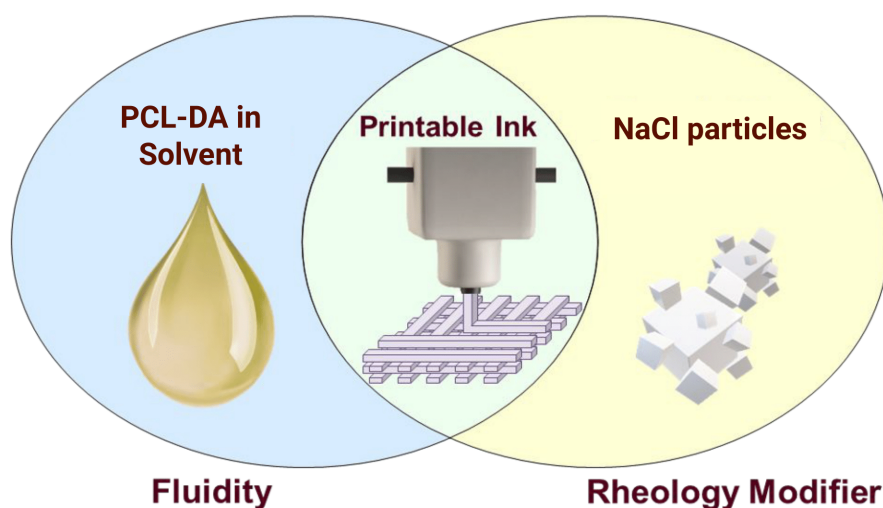
Figure 3.1: Schematic illustrating polymer and NaCl particles together contributing to rheology in DIW ink.

3.2 Experimental Details

3.2.1 Materials

Polycaprolactone-diacrylate (PCL-DA) used for the printing operations was obtained from Brandon Nitschke in the Grunlan research group at Texas A&M University, and the synthesis method was based on the protocol as previously reported. [18] The synthesis steps are discussed in detail in Appendix B. The following chemicals were obtained from the following manufacturers and used as is: sodium chloride (NaCl) and dimethylformamide (DMF) from Fisher chemical, chloroform from Supelco, 2,2-Dimethoxy-2 -phenylacetophenone (DMP) from TCI chemicals, dichloromethane (DCM) from Sigma-Aldrich, and tetrahydrofuran (THF) from JT Baker.

3.2.2 Instrumentation

The 3D printing was performed on a Hyrel 3D Engine SR with an SDS-10 syringe extrusion head. Fourier transform infrared spectroscopy measurements were carried out using FT/IR-4600 FT-IR Spectrometer. Scanning electron microscopy (SEM) images were taken using a TESCAN VEGA SEM with an accelerating voltage of 10 kV. SEM samples were sputter coated with 5 nm of Au. The SEM was located in TAMU Microscopy & Imaging Center. Energy dispersive X-ray spectroscopy (EDS) measurements were taken from JEOL JSM-7500F equipped with an Oxford EDS system equipped with X-ray mapping and digital imaging. Thermogravimetric analysis was carried out using TA Instruments TGA 5500 and Differential scanning calorimetry was carried out using TA Instruments DSC 2500. Rheological properties were analyzed using a TA Instruments DHR-2 Rheometer with a 25 mm parallel plate and Dynamic mechanical analysis measurements were performed using TA Instruments DMA 850. All the above-said instruments were located at the Soft Matter facility, TAMU.

3.3 Methods

3.3.1 Ink Formulation

The solvent choice for the ink had to be made under various considerations. While the complete dissolution of polymer in the solvent is required, most of the solvents that can dissolve polycaprolactone diacrylate are volatile and hence not suitable for keeping the ink stable long enough for printing. These are solvents like chloroform, dichloromethane, and toluene that provide partial to complete dissolution. On the other hand, the solvent is required to not dissolve NaCl and allow its operations as a rheology modifier.

Solvents like dimethylformamide (DMF) and N-Methyl-2-pyrrolidone (NMP) are capable of dissolving PCL-DA under elevated temperatures of ~ 40°C and not dissolving NaCl. Also, these solvents being miscible with water could be washed away alongside NaCl, ensuring the removal of these non-volatile components from the system post-printing. Considering the toxicity of NMP, DMF was adopted as our ink solvent. However, to improve the solubility of the polymer at room temperature, small amounts of chloroform were included.

To facilitate the curing of printed structures, the addition of a photoinitiator is essential. In the absence of the same, the ink fails to cure and when used in excess, the prints over cure to lose shape memory. Hence, the amount of photoinitiator had to be optimized so that it does not interfere with the shape memory properties by making the structures too rigid through over-curing but still ensures crosslinking between the polymers.

3.3.2 Direct Ink Writing

The optimum design revised for the bone scaffolds includes a small cylindrical puck with macropores the size of 200-300 microns and micropores the size of 20-30 microns. The print designs are generated using the software PrusaSlicer and the pucks generated here contains a perimeter and a rectilinear pattern of 15% infill on the base cylindrical shape. The macropores are aimed to achieve tissue integration in the scaffolds and the micropores are responsible for fluid penetration and bulk degradation properties. The infill percentage and the nozzle size are optimized in

accordance to the macropore size in the print design. Further details on the G-code generation for printing and curing are given in Appendix B.

3.3.3 Rheometry Parameters

Rheology measurements were carried out to study the viscosity, modulus, and thixotropy properties corresponding to the polymer solution (without salt) and the ink (with salt). Viscosity measurements were carried out at a shear rate ranging from 10^{-3} to 10^3 s^{-1}. However, the initial data at lower shear rates were excluded as it primarily reflects the time taken for the samples to reach stable behavior. During modulus measurements, the samples were subjected to an oscillation strain from 10^{-3} to 10^3% to analyze the variations in storage and loss modulus measurements with the strain increase. Finally, during thixotropy measurements, the viscosity of the samples was measured over time as the shear rate was varied through three steps: 0.5 s^{-1} maintained for 720 seconds, followed by a shear rate of 1.0 s^{-1} for 60 seconds, and back to the 0.5 s^{-1} shear rate for 240 seconds. The viscosity variations in the samples during these steps were analyzed.

To perform rheology measurements, the upper parallel plate of the rheometer was raised to a loading height of 8 cm. Then, approximately 1.2 ml of the polymer solution or ink specific to each experiment was dispensed onto the lower measuring plate. The upper plate was subsequently lowered to a height equivalent to 1020 μm, which squeezed any excess sample out through the sides of the plate. Careful removal of the excess sample was followed by lowering the upper plate further to a 1000 μm gap, where all experiments were conducted. The results presented are the average of data obtained from three different sets that were in agreement with each other.

3.4 Results

3.4.1 Ink Composition

The inks for DIW were developed through trial and error, using varying proportions of solvents, polymers, and sodium chloride particles (<38 microns in size). While the ink shall not flow through the syringe when held, it must be smoothly extruded upon the application of a small stress from the DIW printer (i.e., it should be shear thinning and thixotropic). The composition given in Table 3.1

provided the most optimal properties taking into account rheology, printing ease, curing efficiency, and washing abilities.

Component	Weight/Calculation
PCL-DA	0.5 gram
NaCl	1.25 grams
DMF	0.6 ml
CHCl$_3$	0.3 ml
DMP	25milligrams $\rightarrow$ 5 wt% of polymer
Porosity	$= \dfrac{1.25 \text{ grams}}{1.25 + 0.5 \text{ grams}}$ $= 83.33\%$

Table 3.1: Ink composition for direct ink writing

3.4.2 Rheology Measurements

The ink prepared was first studied for its rheological compatibility with regards to DIW. PCL-DA dissolved in the solvent combination of DMF and CHCl$_3$ is compared with and without the sodium chloride particles added. The Newtonian behavior of the polymer solution, maintaining a constant viscosity against an increasing shear rate can be seen against the shear-thinning behavior of ink with a reducing trend of viscosity in Figure 3.2 (a). While the polymer solution maintains a constant viscosity of 100-200 mPa.s across all shear rates, the ink undergoes a drop in its viscosity from 10^6 to 10^3 mPa.s as the shear rate increases from 10^{-1} to 10^3 s^{-1}. This indicates how the addition of NaCl particles modifies the rheology of the polymer solution to make it shear thinning, and capable of being extruded.
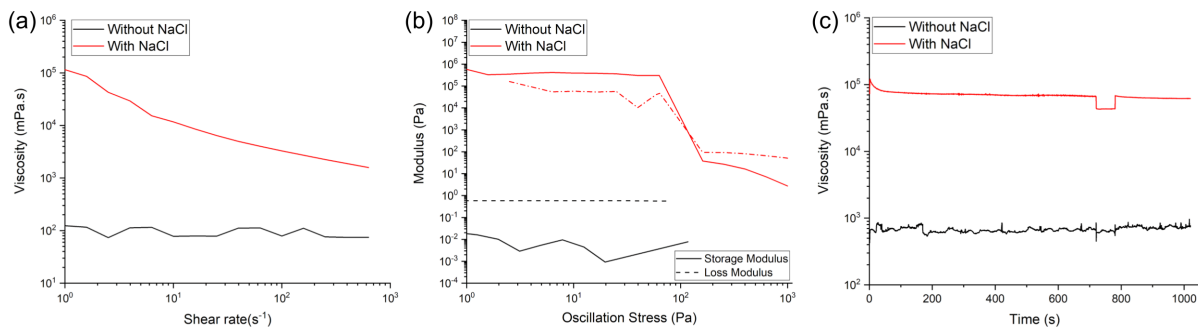
Figure 3.2: (a) Viscosity, (b) modulus, and (c) thixotropy (left to right) measurements of the polymer solution vs ink.

The modulus and thixotropy variations in the ink through this NaCl addition are also inspected. Figure 3.2 (b) shows the modulus variations in the polymer solution vs the ink with an oscillation stress sweep. The polymer solution is observed to maintain its loss modulus higher than the storage modulus across the stress variations. This is an indication of how the polymer solution behaves like a liquid at all times regardless of the stress applied to it. However, in an oscillation stress sweep test on the ink, the storage modulus was initially observed to be higher than the loss modulus, but a reversal occurred around 100 Pa stress resulting in the loss modulus becoming higher than the storage modulus. This is indicative of how the viscoelastic ink exhibits a solid-like behavior when in the syringe, whereas it transforms into a viscoelastic liquid during extrusion. Thus these results reaffirm the shear thinning behavior induced by NaCl particles in the polymer solution.

The data shown in Figure 3.2 (c) indicates the thixotropic behavior of the salt-containing ink. The viscosity of the polymer solution without salt remains constant at $\sim$500 mPa.s, across variations in shear rate, similar to its native viscosity. However, while the ink maintains a viscosity equivalent to $\sim 8 \times 10^4$ mPa.s in the initial phase of a 0.5 s^{-1} shear rate, the viscosity drops to 4 $\times 10^4$ mPa.s during the 1.0 s^{-1} shear rate but only to regain it back when the shear rate is reversed. This is indicative of the ability of the ink to behave back as a viscoelastic solid post extrusion during the short span of which it exhibits a liquid-like behavior. Overall, the addition of NaCl brings many properties suitable for direct ink writing in this polymer, as evidenced by the combined viscosity, modulus, and thixotropy measurements on both the polymer systems with and without NaCl.

3.4.3 Printing and Curing Operations

The design for the print involves a cylindrical structure as a base, which incorporates a rectilinear infill pattern in it. A cylindrical shape is commonly used in bone tissue engineering because it closely resembles the shape and structure of long bones in the human body. By using this design, the mechanical stress is expected to be evenly distributed throughout the scaffold, which aids in the growth and development of bone tissue from stem cells. The design development for the printing process is depicted in Figure 3.3.
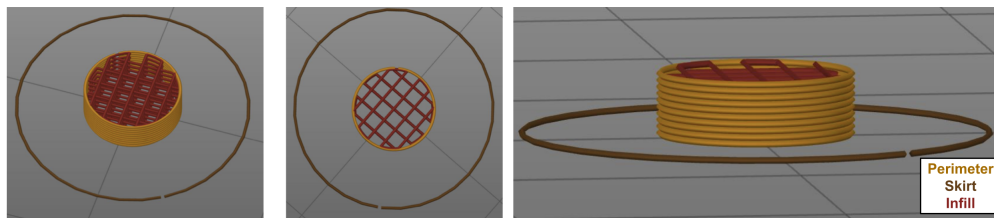
Figure 3.3: Print design generated using PrusaSlicer including a skirt, perimeter, and infill

The printing was carried out using a 22G nozzle (0.413 ± 0.019 mm diameter) to achieve the intricate structures required for the puck, as shown in Figure 3.4 (a). Curing is carried out by a UV light torch of wavelength 365 nm, which traces the perimeter of the pucks after each layer is extruded as shown in Figure 3.4 (b) (i.e., print-cure, print-cure, etc.). To start the printing smoothly and get rid of initial extrusion non-uniformities, a skirt is added around the print design, detached from the actual design, and later discarded. After printing the skirt, the perimeter of the puck is printed, followed by the infill pattern. The liquid ink retains the printed scaffold structure through cross-links generated via UV curing as shown in Figure 3.4 (c). The addition of a photoinitiator to the ink aids in this process and the white color of the ink is supposed to increase the depth of curing against a dark-colored ink. [23] The subsequent runs proceed without a skirt, to avoid further waste of ink. The parameters followed for DIW prints are summarized in Table 3.2. Additional prints carried out through DIW employing different sizes of nozzles and layer heights are depicted in

Appendix B.
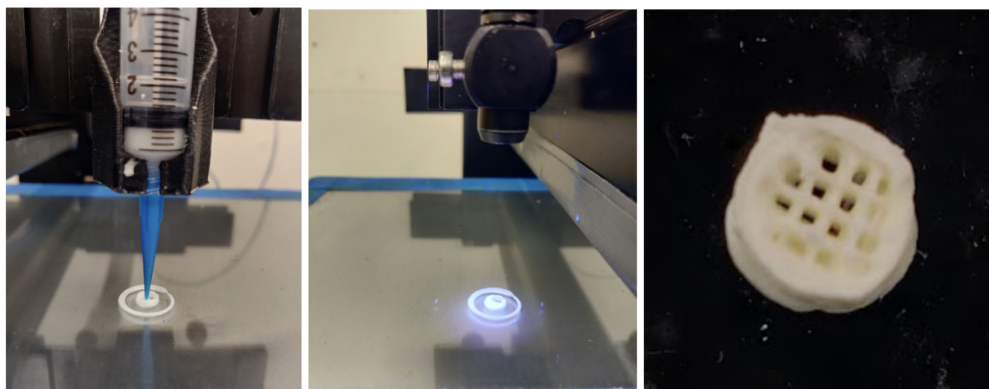
Figure 3.4: (a) Direct Ink Writing Process, (b) Curing, (c) Final product.

DIW Parameters	Value
Nozzle	22G 0.413 ± 0.019 mm inner diameter
Layer Height	0.2 mm
Skirt	1 layer, 1 loop, 4 mm from object
Perimeter	1 layer
Horizontal/Vertical shells	5
Print Speed, Travel Speed	2 mm/min
Estimated Printing Time	6 mins 58 secs
Infill pattern	Rectilinear, 15%

Table 3.2: DIW printing parameters

3.4.4 Post Printing Processes

Washing of the printed structures was carried out using distilled water to remove the NaCl crystals and any amount of additional solvents remaining in the system. As explained before, the

choice of solvents is made in a way they are all miscible with water if non-volatile and can no longer remain in the final product, post the washing step. Post-printing the dried structures were weighed before and after washing. The printed pucks underwent a washing process using water and a small amount of THF. The pucks were placed in a beaker filled with 100-200 ml of water and stirred on a hotplate at 300-400 rpm. The water was changed regularly, and towards the end of the process, 2-3 ml of THF were added. The addition of THF helps the structure swell slightly and hence removes salt particles from the inner pores. The weight of the printed pucks measured in the dry state is compared to the weight of the printed structures post-salt removal and drying. The weight difference matching the theoretical calculation performed according to the weight of components in the ink confirms the removal of salt from the system.

After ensuring all the salt particles are washed out (based on weight differences), the structures are dried in the vacuum oven and further annealed at 85°C for an hour. This step enhances the shape memory properties of the printed structures (as previously observed in cast structures). [18] However, annealing can sometimes lead to collapsing or shrinking of pores. The same is illustrated in Figure 3.5. Hence, annealing of the samples was performed with sodium chloride during the pre-drying stage, and the washing was carried out afterward.

Figure 3.5: Printed structures salt removed post annealing (top) compared to printed structures annealed post-salt removal (bottom)

Although characterizations are carried out to ensure the curing is proper in the printed struc-

tures, a chemical immersion test is performed to get a holistic understanding of curing in the entire printed structure and establish how much polymer is not incorporated into the structure through chemical cross-linking. Each printed structure is immersed in a vial containing 10 ml of dichloromethane and left to stir for 48 hours at 200 rpm in a tabletop shaker. The samples are observed to swell completely in DCM solvent and are then air-dried and weighed again. The weight loss during this step is considered to be the uncured portions and the curing time and photoinitiator % are optimized based on this to keep the uncured portions at a minimum. For the printed structures obtained, this cured proportion comes out to be around 85%.

3.4.5 Crosslinking and Porosity

The printed structures were characterized to inspect the efficiency of curing via DIW and annealing, porosity via salt removal, and shape memory. Fourier transform infrared (FTIR) spectroscopy was used to characterize the ink before printing as well as the printed structures after the salt removal and annealing stages to observe the effect of curing. The C=C stretching peaks at 1669 cm^{-1} and C=C bending peak at 665 cm^{-1} present in the ink are observed to vanish after the printing and curing steps as shown in Figure 3.6. This is indicative of how the double bonds in the acrylate groups on either end of PCL-DA open up to crosslink between the polymers during printing. This confirms the efficient curing of PCL-DA. Although FTIR provides valuable information about surface properties, it cannot provide a comprehensive analysis of the bulk properties. Hence, multiple runs were carried out on the surface as well as cross-sections of the printed structures to confirm the same.
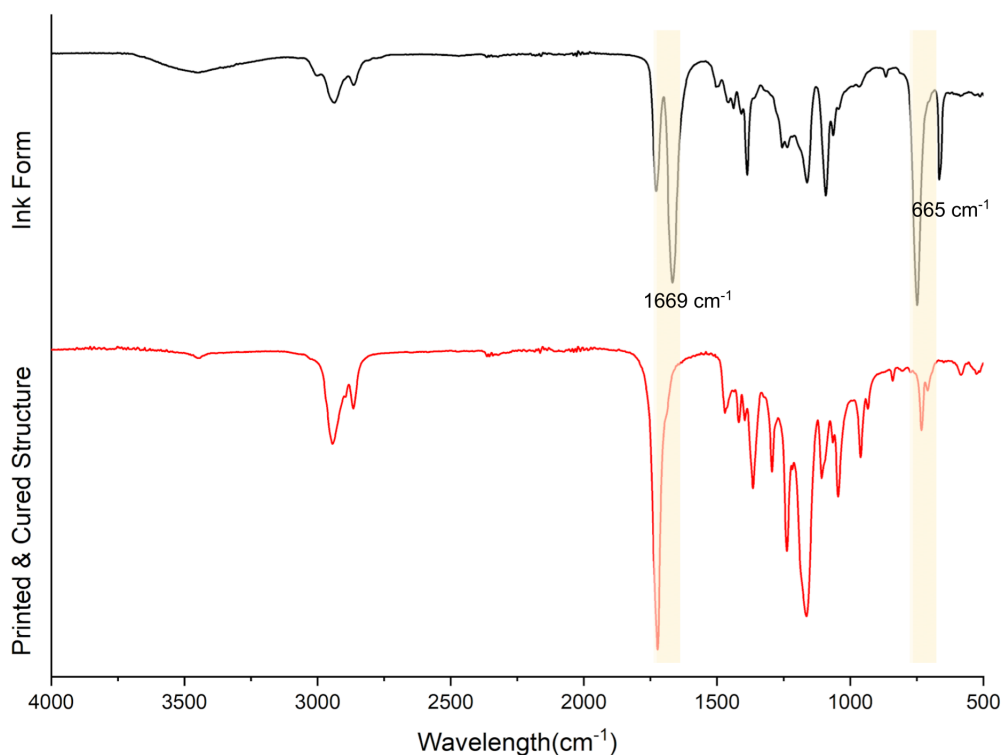
Figure 3.6: FTIR Spectra of the ink used for printing vs printed and cured structure

For ensuring the removal of sodium chloride and generation of pores, scanning electron microscopy (SEM) images are captured and electron dispersive spectroscopy (EDS) is conducted on the prints. For SEM and EDS measurements, samples were made from the cross-section of the printed structures before and after salt removal. Samples were sliced using a disposable scalpel and the cross section is 5 nm coated with gold (Au) to avoid potential charging during the analysis. Due to the ductile nature of PCL-DA, scalpel marks were left on the material's cross-sections during cutting, which hindered the visibility of NaCl crystals or pores according to the stage in washing. To address this issue, the pucks were frozen prior to slicing by dipping them in liquid nitrogen. This process made the pucks hard and brittle for a short period, which facilitated clean slicing without leaving any marks. As given in Figure 3.7, the printed structures before salt removal clearly show the NaCl crystals in the range of 10 microns, uniformly distributed across the printed structures. After salt removal, uniform pores in the same range of diameter are seen on the cross sections of the samples. The result from SEM is confirmed by the EDS results obtained.

33
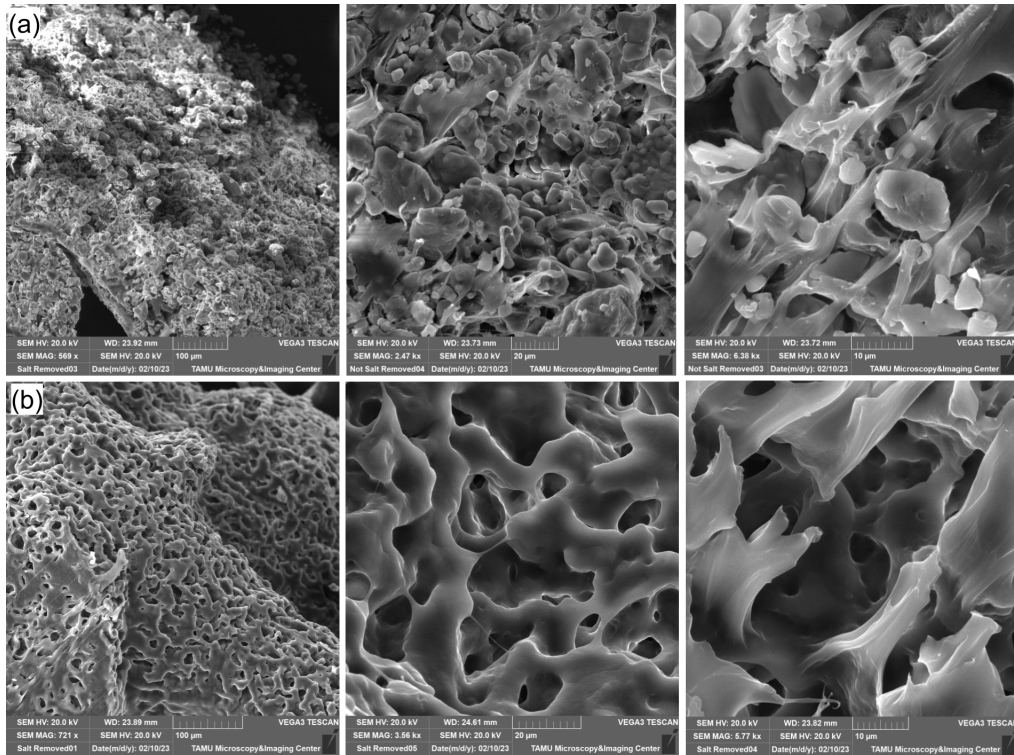
Figure 3.7: SEM Images: (a) Before NaCl removal (top) and (b) after NaCl removal (bottom)

Figure 3.8 shows EDS results from the cross-sectional samples of the printed pucks before and after salt removal. The overlapping of the elemental presence on the SEM images aids in the identification and differentiation of the morphological features within the samples. While the presence of Na and Cl elements can be clearly seen in the samples before salt removal around the NaCl crystals, they almost completely vanished in the samples after salt removal around the pores.
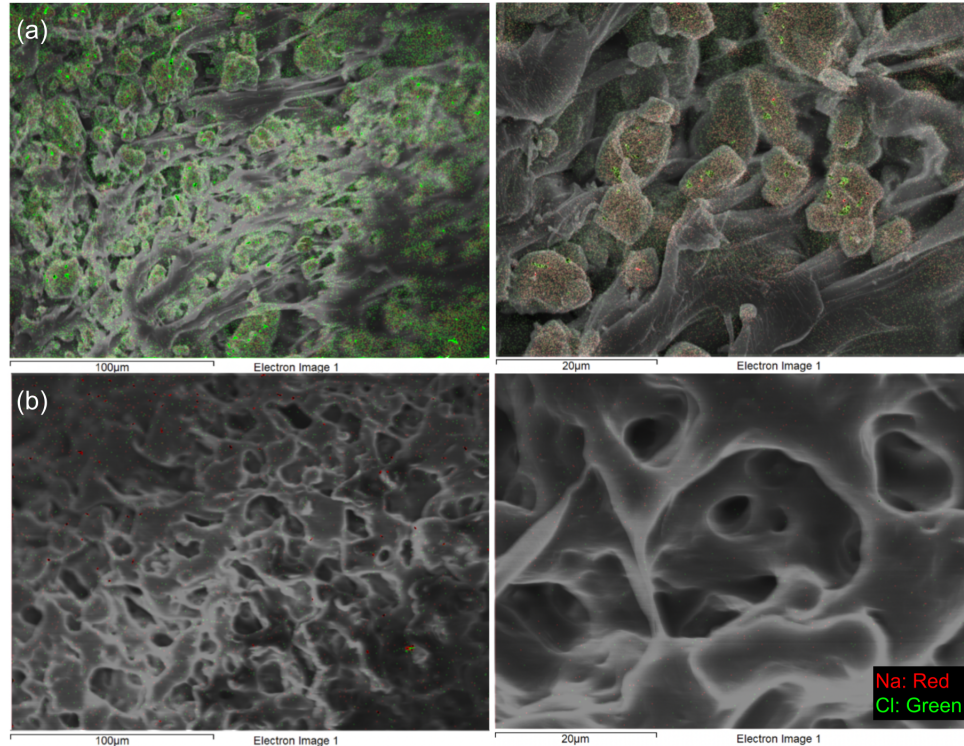
Figure 3.8: EDS elemental analysis overlapped with the corresponding SEM images:
(a) Before NaCl removal (top) and (b) after NaCl removal (bottom).
Green color represents the presence of chlorine and red of sodium in the images above.

3.4.6 Thermal and Shape Memory Properties

The thermogravimetric analysis (TGA) of the printed structures shows a one-step decomposition around 400°C that agrees with the thermal behavior of PCL-DA (Figure 3.9 (a)). This shows how the thermal properties of the polymer are not compromised with the printing process. Following these results, the printed structures were characterized using differential scanning calorimetry (DSC), which gave melting point, again consistent with that of PCL-DA, at 53°C. This is demonstrated in Figure 3.9 (b) through heat flow measured against heating-cooling cycles. Hence, printing does not significantly change the thermal stability of the polymer and the shape memory properties of the prints can be expected around a similar range of temperature.
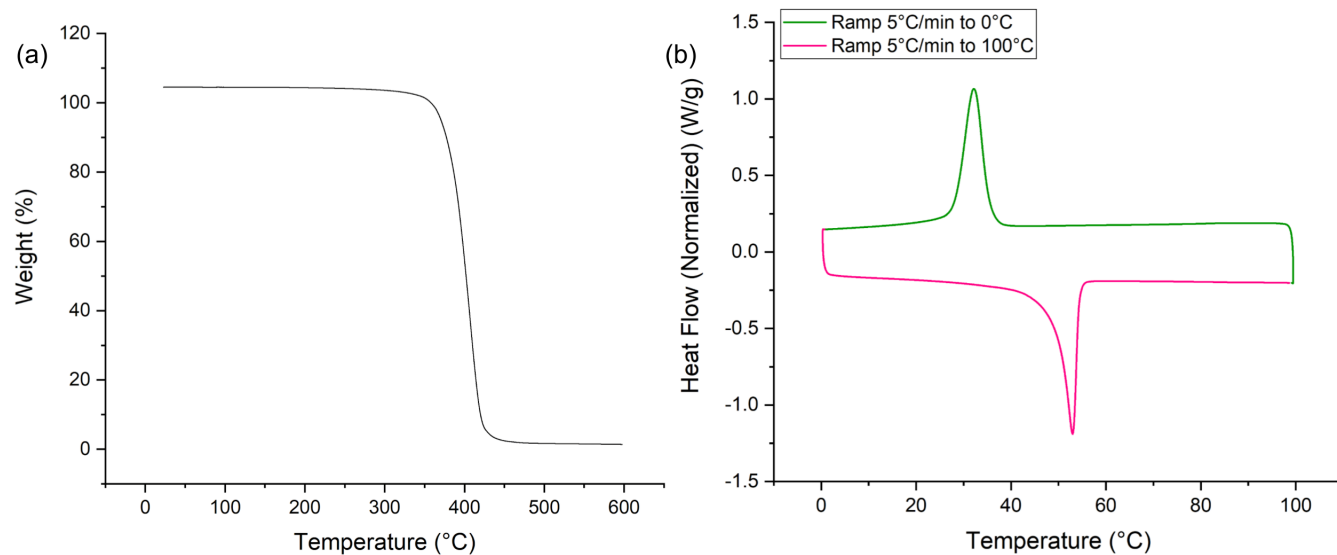
Figure 3.9: (a) TGA plot, (b) DSC plot.

The PCL-DA material is expected to exhibit shape memory properties close to its melting transition temperature. To test this, the printed structures were exposed to a temperature range of ∼53°C, causing them to soften and adopt a different shape. The structures were then immediately dipped in cold water to retain their new shape. Remarkably, the structures retained their altered shapes even when no longer submerged in water and could be returned to their original printed shapes by exposing them to the same temperature range. This suggests that the structures are capable of "remembering" their initial configurations and can return to them under the appropriate conditions. The thermal stimulus for shape memory in PCL-DA occurs around 53°C. Figure 3.10 (a) and (b) denotes the stretching and twisting performed on a DIW PCL-DA lattice structure and the shape recovery that it undergoes when subjected to its characteristic transformation temperature.
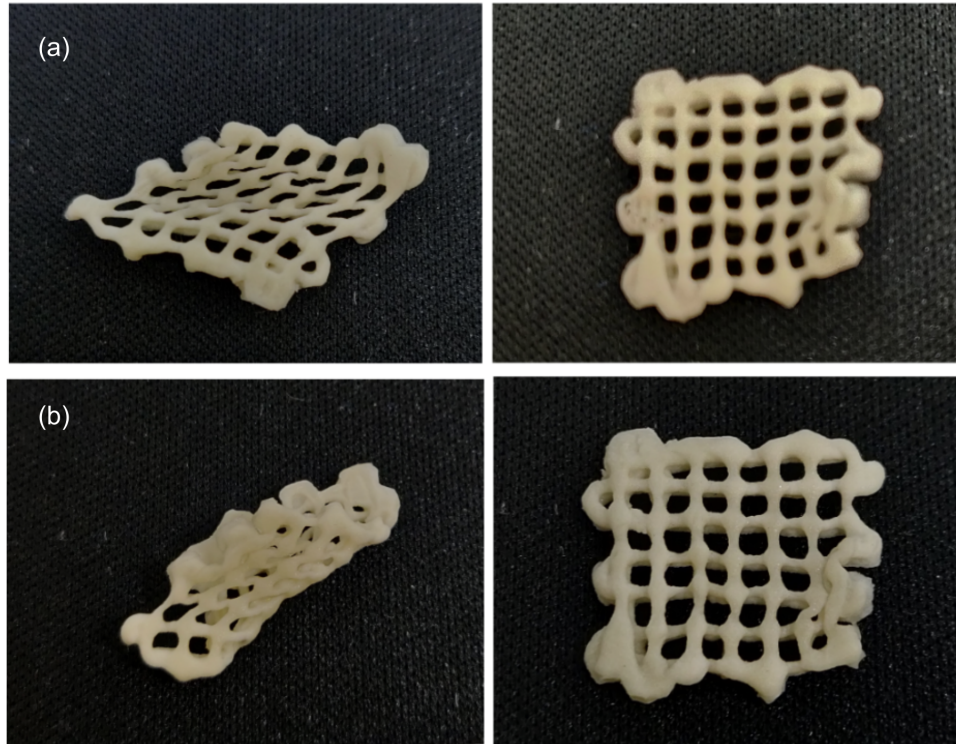
Figure 3.10: Printed structures regaining their shape after (a) stretching (top) and (b) twisting (bottom) actions.

3.4.7   Mechanical Properties

Dynamic mechanical analysis (DMA) of the printed structures was carried out to inspect how the compression modulus of these prints are affected as a result of porosity. The structures were printed in a similar design to the scaffolds, but with no macropores. This means that the vertical and horizontal shells were attached to each other and generated in alternating layers with a higher infill%. While half of the printed samples were made to retain the sodium chloride crystals within them, the other half had them washed away through days and further freeze-dried. Freeze drying was carried out instead of vacuum drying to make sure the pores do not collapse due to vacuum. The DMA setup and samples printed are denoted in Figure 3.11(a) and (b), respectively. Further, the Stress-strain plots of the samples with and without pores are plotted in Figure 3.12 (a) and (b). They are averaged between three similar sets of data acquired. Although they have similar slopes (i.e, compression modulus values), the sample with pores has a slightly higher modulus. These

are preliminary results at the moment, and has potential for improvement through variations in processing.

Figure 3.11: (a) DMA compression modulus setup and (b) Printed samples for the study.

Figure 3.12: Stress vs strain plot of DIW structures with and without NaCl

4. CONCLUSIONS AND FUTURE DIRECTIONS

4.1 Langmuir Blodgett Studies of Alkylated Graphene Oxide Nanosheetss
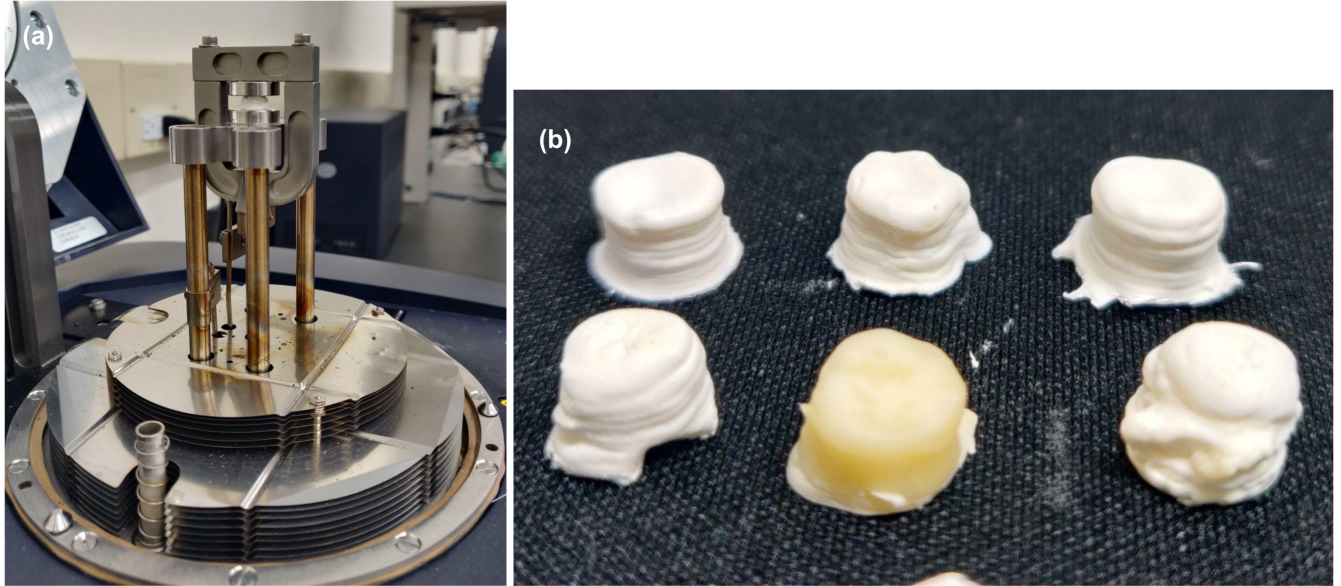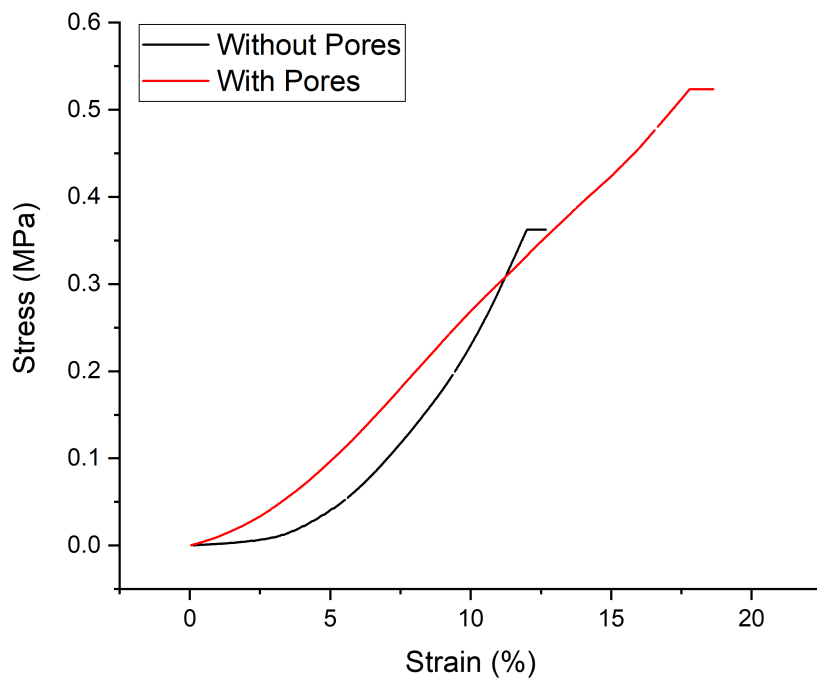
In this study, the behavior of alkylated and reduced graphene oxide nanosheets was studied on the air-water interface in a Langmuir Blodgett trough. The variations generated in the pressure isotherms under different solvents of dispersion, alkyl chain lengths, subphase pH, and subphase ionic concentrations were studied.

LB measurements are generally carried out using samples dispersed in volatile solvents. This way, the dispersion medium evaporates immediately, contributing to the formation of a monolayer of the dispensed particles/nanosheets at the air-water interface. According to the results obtained, however, it is observed that there still exists a difference in the nanosheet interfacial behavior past solvent removal even within volatile solvents. This shows how the solvent of dispersion of the alkylated GO leaves a lasting impact on their behavior. The variations generated by alkyl chains attached to the GO nanosheets were also studied alongside the solvents to identify the common trend ruling the nanosheet behavior. However, these results did not indicate a clear pattern as the surface pressure isotherms were observed to be impacted by an amalgamation of factors. Graphene oxide and its inability to be quantified at a molecular level greatly interfere with the aim of identifying a pattern in the behavior of these nanosheets.

Further, moving on to the subphase medium effects, shifting the pH of the subphase to acidic and basic regimes from neutral was seen to create different impacts on C9-GO and rGO samples, the behavior varying further with the solvent of dispersion. This was attributed to different ions generated in the buffer solutions, their possible electric and steric interactions with the samples, the functional groups present in the nanosheets, the shielding effect by the alkyl chains, and so on. To simplify the parameters involved in this system, variations in ionic concentration was generated in the subphase with the help of sodium chloride. While rGO in DMF showed a stable pattern with the addition of salt, C9-GO and later MXenes showed no difference in behaviors.

Overall, an actual comparison between the LB trough interface to an emulsion system goes a long way. Further simplification of the system in the study through the elimination of many influencing parameters might be necessary to reach any meaningful conclusion that can be reflected in a working emulsion. On the other hand, shifting to a different system like a Goniometer to conduct actual liquid-liquid interfacial studies would be more beneficial to draw parallels with an emulsion system.

4.2 Direct Ink Writing of Shape Memory Polymers

In this study, direct ink writing is successfully employed to print porous shape memory polymers for bone scaffold applications. The use of sacrificial NaCl filler in DIW ink is proven to be a viable method for generating porosity in PCL-DA (known for its shape memory properties) structures while also modifying the rheology of the ink to suit printing. This innovative technique has the potential to revolutionize various fields, including biomedical engineering, where porous structures are highly desirable for applications such as tissue engineering and drug delivery. Further studies are needed to explore the full potential of this technique and its applications in various fields.

DIW ink was devised via employing removable solvents to dissolve the polymer, using NaCl crystals to modify the rheology, and through addition of a photoinitiator to enable curing operations. Cylindrical scaffold prints were achieved through careful calculations of print design inculcating suitable sizes of filler and print layer height. The efficiency of the printing method is confirmed through the ability to optimize the porous structure deemed in the form of macropores and micropores. While macropores can be attained through the flexibility in direct ink writing, micropores are made possible through modifying the filler size. The prints generated were shown to have attained macropores between the cylindrical infill and uniform micropores after complete NaCl removal. The structures attained 85% curing and were shown to maintain stable thermal properties equivalent to the polymer. Eventually, the prints also exhibited efficient shape memory properties and promising mechanical properties with regard to porosity.

In the future, further modifications can be made to the ink to improve its osteoinductive, degradation behaviors which would improve the efficiency of the implants. Also, in the future, having achieved macropores through more complicated geometries, NaCl filler can be substituted with non-sacrificial fillers like capsules that can carry a liquid of choice. Thus, the printed structures can be made to carry medicinal fluids or other useful minerals that could be released into the body as the scaffold degrades. [23]

REFERENCES

[1] "Langmuir & Langmuir Blodgett | Measurements."

[2] B. Rodier, A. de Leon, C. Hemmingsen, and E. Pentzer, "Controlling Oil-in-Oil Pickering-Type Emulsions Using 2D Materials as Surfactant," *ACS Macro Letters*, vol. 6, pp. 1201–1206, Nov. 2017. Publisher: American Chemical Society.

[3] Q. Luo, Y. Wang, E. Yoo, P. Wei, and E. Pentzer, "Ionic Liquid-Containing Pickering Emulsions Stabilized by Graphene Oxide-Based Surfactants," *Langmuir*, vol. 34, pp. 10114–10122, Aug. 2018. Publisher: American Chemical Society.

[4] K. Ariga, Y. Yamauchi, T. Mori, and J. P. Hill, "25th Anniversary Article: What Can Be Done with the Langmuir-Blodgett Method? Recent Developments and its Critical Role in Materials Science," *Advanced Materials*, vol. 25, pp. 6477–6512, Dec. 2013.

[5] H. Chou, C.-T. Chen, K. F. Stork, P. W. Bohn, and K. S. Suslick, "Langmuir-Blodgett Films of Amphiphilic Push-Pull Porphyrins," *The Journal of Physical Chemistry*, vol. 98, pp. 383–385, Jan. 1994.

[6] G. Wen, B. Chung, and T. Chang, "Effect of spreading solvents on Langmuir monolayers and Langmuir–Blodgett films of PS-b-P2VP," *Polymer*, vol. 47, pp. 8575–8582, Dec. 2006.

[7] M. Meszaros, A. Eisenberg, and R. Bruce Lennox, "Block copolymer self-assembly in two dimensions: nanoscale emulsions and foams," *Faraday Discussions*, vol. 98, no. 0, pp. 283–294, 1994. Publisher: Royal Society of Chemistry.

[8] L. J. Cote, F. Kim, and J. Huang, "LangmuirBlodgett Assembly of Graphite Oxide Single Layers," *Journal of the American Chemical Society*, vol. 131, pp. 1043–1049, Jan. 2009. Publisher: American Chemical Society.

[9] Q. Zheng, L. Shi, P.-C. Ma, Q. Xue, J. Li, Z. Tang, and J. Yang, "Structure control of ultra-large graphene oxide sheets by the Langmuir–Blodgett method," *RSC Advances*, vol. 3,

no. 14, pp. 4680–4691, 2013. Publisher: Royal Society of Chemistry.

[10] D. D. Kulkarni, I. Choi, S. S. Singamaneni, and V. V. Tsukruk, "Graphene OxidePolyelectrolyte Nanomembranes," *ACS Nano*, vol. 4, pp. 4667–4676, Aug. 2010. Publisher: American Chemical Society.

[11] Y. Yang, X. Yang, W. Yang, S. Li, J. Xu, and Y. Jiang, "Ordered and ultrathin reduced graphene oxide LB films as hole injection layers for organic light-emitting diode," *Nanoscale Research Letters*, vol. 9, p. 537, Oct. 2014.

[12] Q. Huo, S. Russev, T. Hasegawa, J. Nishijo, J. Umemura, G. Puccetti, K. C. Russell, and R. M. Leblanc, "A Langmuir Monolayer with a Nontraditional Molecular Architecture," *Journal of the American Chemical Society*, vol. 122, pp. 7890–7897, Aug. 2000. Publisher: American Chemical Society.

[13] Y.-J. Wang, U.-S. Jeng, and S.-H. Hsu, "Biodegradable Water-Based Polyurethane Shape Memory Elastomers for Bone Tissue Engineering," *ACS biomaterials science & engineering*, vol. 4, pp. 1397–1406, Apr. 2018.

[14] X. Zhai, Y. Ma, C. Hou, F. Gao, Y. Zhang, C. Ruan, H. Pan, W. W. Lu, and W. Liu, "3D-Printed High Strength Bioactive Supramolecular Polymer/Clay Nanocomposite Hydrogel Scaffold for Bone Regeneration," *ACS Biomaterials Science & Engineering*, vol. 3, pp. 1109–1118, June 2017. Publisher: American Chemical Society.

[15] D. Zhang, O. J. George, K. M. Petersen, A. C. Jimenez-Vergara, M. S. Hahn, and M. A. Grunlan, "A bioactive "self-fitting" shape memory polymer scaffold with potential to treat cranio-maxillo facial bone defects," *Acta Biomaterialia*, vol. 10, pp. 4597–4605, Nov. 2014.

[16] J. M. Williams, A. Adewunmi, R. M. Schek, C. L. Flanagan, P. H. Krebsbach, S. E. Feinberg, S. J. Hollister, and S. Das, "Bone tissue engineering using polycaprolactone scaffolds fabricated via selective laser sintering," *Biomaterials*, vol. 26, pp. 4817–4827, Aug. 2005.

[17] H. Eftekhari, A. Jahandideh, A. Asghari, A. Akbarzadeh, and S. Hesaraki, "Histopathological Evaluation of Polycaprolactone Nanocomposite Compared with Tricalcium Phosphate in Bone Healing," *Journal of Veterinary Research*, vol. 62, pp. 385–394, Dec. 2018.

[18] M. R. Pfau, K. G. McKinzey, A. A. Roth, L. M. Graul, D. J. Maitland, and M. A. Grunlan, "Shape memory polymer (SMP) scaffolds with improved self-fitting properties," *Journal of Materials Chemistry B*, vol. 9, no. 18, pp. 3826–3837, 2021.

[19] H. Baniasadi, R. Ajdary, J. Trifol, O. J. Rojas, and J. Seppälä, "Direct ink writing of aloe vera/cellulose nanofibrils bio-hydrogels," *Carbohydrate Polymers*, vol. 266, p. 118114, Aug. 2021.

[20] E. A. Guzzi, R. Bischof, D. Dranseikiene, D. V. Deshmukh, A. Wahlsten, G. Bovone, S. Bernhard, and M. W. Tibbitt, "Hierarchical biomaterials via photopatterning-enhanced direct ink writing," *Biofabrication*, vol. 13, Sept. 2021.

[21] R. Ajdary, G. Reyes, J. Kuula, E. Raussi-Lehto, T. S. Mikkola, E. Kankuri, and O. J. Rojas, "Direct Ink Writing of Biocompatible Nanocellulose and Chitosan Hydrogels for Implant Mesh Matrices," *ACS Polymers Au*, vol. 2, pp. 97–107, Apr. 2022. Publisher: American Chemical Society.

[22] C. E. Cipriani, T. Ha, O. B. Martinez Defilló, M. Myneni, Y. Wang, C. C. Benjamin, J. Wang, E. B. Pentzer, and P. Wei, "Structure–Processing–Property Relationships of 3D Printed Porous Polymeric Materials," *ACS Materials Au*, vol. 1, pp. 69–80, Sept. 2021.

[23] C. E. Cipriani, N. C. Starvaggi, K. J. Edgehouse, J. B. Price, S. L. Vivod, and E. B. Pentzer, "Additive manufacturing: modular platform for 3D printing fluid-containing monoliths," *Molecular Systems Design & Engineering*, vol. 7, no. 9, pp. 1039–1044, 2022. Publisher: Royal Society of Chemistry.

[24] P. Wei, G. A. Bhat, C. E. Cipriani, H. Mohammad, K. Schoonover, E. B. Pentzer, and D. J. Darensbourg, "3D Printed CO2-Based Triblock Copolymers and Post-Printing Modification,"

Angewandte Chemie International Edition, vol. 61, no. 37, p. e202208355, 2022. _eprint: https://onlinelibrary.wiley.com/doi/pdf/10.1002/anie.202208355.

[25] H. Cao, M. Escamilla, K. D. Arole, D. Holta, J. L. Lutkenhaus, M. Radovic, M. J. Green, and E. B. Pentzer, "Flocculation of MXenes and Their Use as 2D Particle Surfactants for Capsule Formation," *Langmuir*, vol. 37, pp. 2649–2657, Mar. 2021.

[26] J. Glazer, M.Z. Dogan, *Trans. Faraday Soc.*, vol. 49, p. 448, 1954.

APPENDIX A

INTERFACIAL STUDIES OF ALKYLATED GRAPHENE OXIDES USING LANGMUIR
BLODGETT

A.1 Graphene Oxide Synthesis

Graphene oxide (GO) synthesis was carried out using the modified Hummer's method (the steps involved are demonstrated in Figure A.1. 1 gram of graphite flakes was added to a conical flask along with 134 ml of sulfuric acid and was left to stir at 300 rpm, maintaining the temperature at a range of 23-25ºC. The mixture was further oxidized with the help of potassium permanganate ($KMnO_4$), added in trips of 1 gram separated by 24 hours to a final amount of 4 grams, while the mixture was allowed to react for this entire period. The end of the reaction is marked by an evident change in solution color to purple and an increase in viscosity to denote successful oxidation. Later, the entire mixture was poured into 800 ml of cold water (approximately 700 ml of the measuring cylinder filled with ice cubes, made to 800 ml with water), very slowly. Now, hydrogen peroxide was added to the beaker to arrest the process of oxidation, dropwise until the purple solution turned to a tortilla brown and no more bubbles appeared from the solution on further addition of the peroxide.

The synthesized graphene oxide was further washed in isopropanol in multiple steps of centrifugation. The supernatant was discarded each time and replaced by more isopropanol through rounds of washing. The washing of nanosheets was carried out until the pH of graphene oxide came down to neutral from acidic. Once the pH was balanced, the sample was dried in a vacuum oven. To facilitate better drying, the bigger chunks were broken in a blender to smaller pieces after partial drying.

Figure A.1: Stages involved in the synthesis of GO (a) Reaction of graphite, sulfuric acid, and potassium permanganate mixture (oxidation), (b) Mixture post-hydrogen peroxide addition (oxidation arrested), (c) Graphene oxide washing (centrifugation), (d) Final product after complete drying in a vacuum oven.

A.2   Functionalizing Graphene Oxide

Graphene oxide functionalizations were carried out using various alkyl chains to generate different samples. 96 mg of GO was sonicated to disperse in 36 ml of dimethylformamide (DMF). In a round bottom flask, 0.0067 moles of the respective amine were dispersed in 60 ml DMF and kept to stir at 300 rpm at 60ºC. 0.551 ml of propylamine (molecular weight = 59.11, liquid density= 0.719g/ml), 0.881 ml of hexylamine (molecular weight= 101.19, liquid density= 0.766g/ml), 1.227 ml of nonylamine (molecular weight= 143.27, liquid density= 0.782g/ml), or 1.8057 grams of octadecylamine (molecular weight = 269.509 ml) was added according to the desired functionalization. Further, GO dispersion was added to the flask and stirred overnight at 55ºC and 350 rpm. In the occurrence of the respective amine being insoluble in DMF, a solvent change is performed to toluene. This is the case only for octadecylamine. This is implemented through centrifugation, removing the DMF in the supernatant, and redispersing the sample in toluene. For the smaller alkyl chains, the mixture can be left dispersed in DMF. Later, after the reaction is completed, the prepared sample is washed a few times in the same solvent in which it is finally dispersed before moving on to a separate solvent system that might facilitate better washing in the further stages. A few steps associated with the octadecylamine functionalization are depicted in Figure A.2.
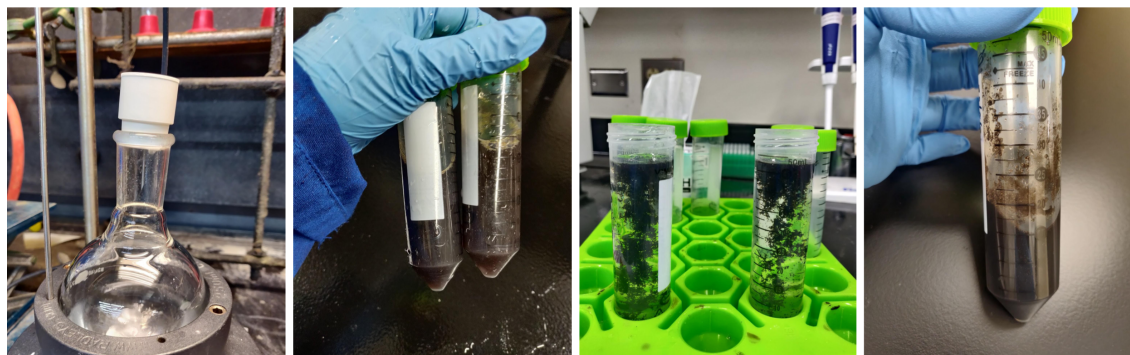
Figure A.2: Stages involved in the octadecylamine functionalization of GO (a) Reaction of GO with octadecylamine, (b) Centrifuging out DMF to redisperse in toluene (c) Centrifugation in chloroform leading to floating, (d) Final dispersion in DMF.

A.3   Synthesis of reduced Graphene Oxide

Reduced graphene oxide (rGO) was synthesized in the same experimental conditions as other alkylated graphene oxides. Again, 0.0067 moles of amine is kept constant for 96 mg of graphene oxide in 60 ml DMF. For triethylamine (molecular weight = 101.19, liquid density= 0.726 g/ml), it is 0.929 ml. Through using triethylamine in the place of other amines and taking the mixture through similar temperature ranges, a mere reduction of GO is expected as triethylamine fails to functionalize GO.

A.4   Small Molecule Removal from Functionalized Graphene Oxide

The presence of any additional small molecules in the nanosheet suspension is a huge concern when it comes to LB studies. Hence any extra amount of amines present in the sample and detached from the nanosheets was washed off in multiple rounds. For graphene oxide functionalized from octadecylamine, a mixture of 1:9 :: chloroform: toluene was used as the dispersant, while for triethylamine, propylamine, hexylamine, and nonylamine, a mixture of 1:2:8 :: chloroform:ethyl acetate:hexane was used in the washing steps. While chloroform and ethyl acetate completely dissolved these amines, hexane helped to separate and settle the functionalized GO. Supernatants from each centrifugation round was collected and analyzed using Fourier transform infrared (FTIR) spectroscopy to ensure they matched with the alkylamine sample (Figure A.3). As highlighted,

the N-H stretching peak at 2850 cm^{-1} and others confirm them to be the same compound. Further, rounds of washing are carried out until the amount of supernatant residue minimized to the least possible.
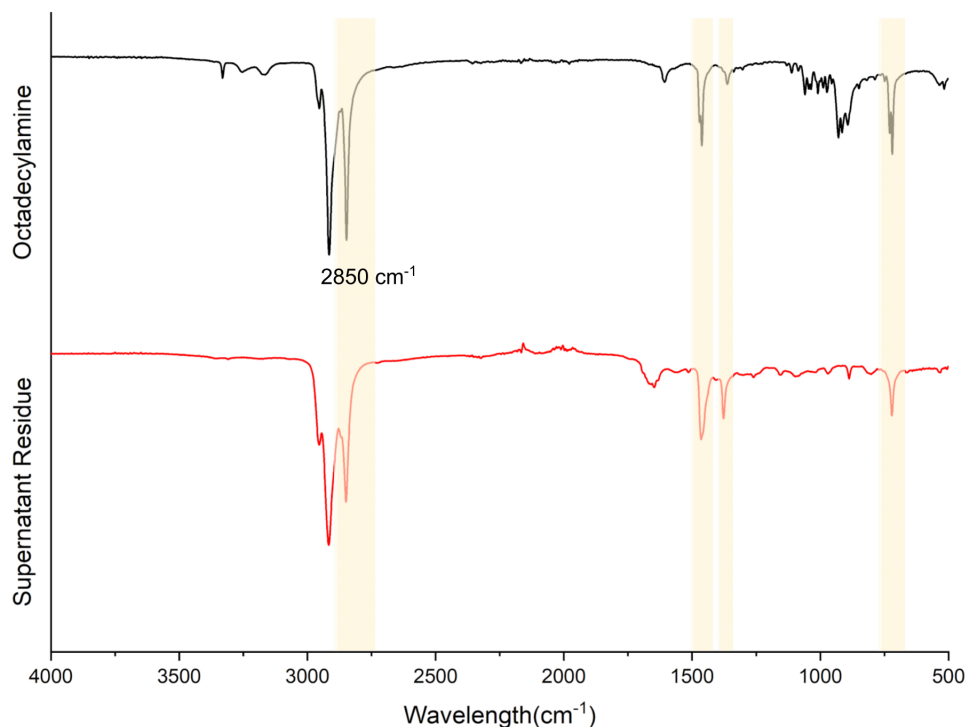

Figure A.3: FTIR spectra of octadecylamine matching with the supernatant.

A.5 Synthesis of Buffer Solutions for LB subphase

An acidic buffer with a pH of 4.4 and a basic buffer with a pH of 10.2 was synthesized for the purpose of carrying out the LB experiments. To generate a buffer solution of pH 4, 0.007731 M acetic acid (corresponding to 4.643 grams in a liter) and 0.02269 M sodium acetate (corresponding to 1.861 grams in a liter) were required. The sodium acetate required was simultaneously synthesized from acetic acid and sodium hydroxide, using the following reaction:

$$CH_3COOH \quad + \quad NaOH \quad \rightarrow \quad CH_3COONa \quad + \quad H_2O$$

1.3625 grams   0.907 grams   1.861 grams
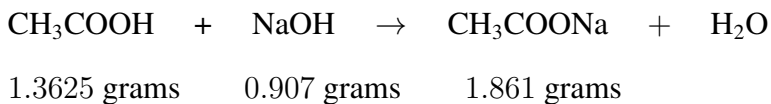
Balancing the reaction appropriately gave 0.907 grams of sodium hydroxide and a total of 4.643 g + 1.3625 g ≈ 6 grams of acetic acid to be the final quantities required for the buffer. Corresponding to the same, 6.3 ml acetic acid (1.05 g/ml density) and 0.907 grams of sodium hydroxide were added to 800 ml distilled water, which was later filled to make it 1 liter. The pH was further measured using a waterproof pH Testr 30 pocket tester and confirmed to be 4.4. Each 1 liter of the buffer was used between four LB runs.

Similarly, a basic buffer of pH 10.2 was synthesized by adding 3.876 grams of sodium bicarbonate (0.04614 M) and 5.709 grams of anhydrous sodium carbonate (0.05386 M) to 800 ml of distilled water, further filled up to 1 liter. The pH was confirmed by measuring with a pH meter.

DIRECT INK WRITING OF POROUS SHAPE MEMORY POLYMERS

B.1 Possible Geometries of Printing

Some of the print geometries generated using the PCL-DA + NaCl ink are given in Figure B.1 below. They are achieved through nozzles ranging from 25G to 16G with the inner diameters varying through 0.26 mm to 1.2 mm.

Figure B.1: Cylindrical and lattice geometries printed using different sized nozzles